

Corso di Laurea Magistrale in
Ingegneria Aerospaziale

Tesi di Laurea in Aeroacustica

Jet Noise Modeling and Prediction using Steady RANS Solutions

Candidato:	Relatori:	Correlatori:	A.A.
Francesco Rosano	Prof. G. Pezzella	Dr. M. Barbarino	2021/2022
Matr. A15/0213	Prof. A. Viviani	Dr. F. Petrosino	
	Prof. S. Miller		

Ai miei nonni Luigi e Franco

Acknowledgements

Ringrazio, in primis, il mio relatore, il Professore *Giuseppe Pezzella*, che mi ha sempre spronato portandomi a dare il meglio di me. I suoi incoraggiamenti sono stati per me fondamentali.

Ringrazio gli ingegneri *Mattia Barberino* e *Francesco Petrosino* che mi hanno fornito tutto il loro supporto nella comprensione dell'aeroacustica. Grazie per i vostri saggi consigli e per il tempo che mi avete dedicato.

A special thanks to Professor *Steven Miller*, whose suggestions helped me to complete this work in the best possible way. Thank you for your kindness and your helpfulness.

Ringrazio tutta la mia famiglia che ha contribuito al raggiungimento di questo traguardo. Ringrazio mia *Madre* e mio *Padre* che hanno sempre supportato ogni mia scelta e che hanno saputo darmi i giusti consigli senza mai impormi alcuna decisione; mia *Sorella* che stimo molto e che è stata presente in tutti i momenti di necessità; il mio piccolo *Lucky* senza il quale tale percorso sarebbe stato più pesante del previsto. Grazie per essermi stati sempre vicini. Un sentito ringraziamento anche a mio nonno *Luigi*, ormai lontano, che fin da piccolo ha sempre alimentato la mia passione per queste materie. Grazie per aver sollecitato la mia curiosità concedendomi di smontare e rompere qualunque cosa.

Un ringraziamento a tutti i miei amici che mi sono stati sempre vicini e con i quali ho condiviso momenti di vera spensieratezza.

Un pensiero particolare a *Federico*, mio fratello da sempre, che ha costantemente appoggiato ogni mia azione e che è stato sempre presente. Grazie per tutti i momenti passati insieme e per i mille istanti di felicità.

Infine, anche se non ultimi, desidero ringraziare anche tutti i miei colleghi che hanno reso piacevole e meno stressante il mio percorso di studi.

Ci tengo a ringraziare particolarmente *Vincenzo Romano* che è stato per me prima di tutto un ottimo amico. Grazie per aver fatto parte di questo mio percorso e per aver contribuito enormemente a tale successo.

Contents

List of Figures	III
Nomenclature	VI
Abstract	X
Introduction	XII
1 Computational Fluid Dynamics	1
1.1 Navier-Stokes Equations	3
1.1.1 Mass Conservation Equation	3
1.1.2 Momentum Conservation Equation	4
1.1.3 Energy Conservation Equation	5
1.1.4 Ideal Gas and Sutherland Law	6
1.2 Turbulence	7
1.3 Statistical Analysis and Modeling of Turbulence	10
1.3.1 The RANS Equations	10
1.3.2 Approximations and Modeling	11
1.3.3 Closed Approximated RANS Equations	13
1.3.4 Turbulence Model: $k - \omega$ SST	14
1.4 Fluid Dynamic Test Case	17
1.4.1 Nozzle Geometry	17
1.4.2 Operating Conditions	18
1.4.3 Fluid Dynamics Mesh Generation	20
1.4.4 Results	22
1.4.5 Grid Convergence Study	26
1.4.6 Comparison with Reference Data	29
2 Aeroacoustics Analogy for Jet-Noise Prediction	38
2.1 Mathematical Theory	40
2.1.1 Sources Terms: Mixing Noise	41

2.1.2	Sources Terms: Broad-Band Shock Associated Noise	41
2.1.3	Solution of Aeroacoustics Equations	43
2.1.4	Mixing Noise: Modeling of Auto-correlation Terms .	46
2.1.5	BBSAN: Modeling of Auto-correlation Terms	48
2.1.6	Total Comprehensive Model	52
2.1.7	Integral Scales of Turbulence Definitions	52
3	Acoustic Results	55
3.1	Implementation of Acoustic Solver	56
3.2	Case SMC0003	59
3.3	Case SMC0004	59
3.4	Case SMC0008	60
A	Green's Function	66
B	Green's Function of the inhomogeneous Helmholtz Equation	67
C	How to Present Results	69
	Matlab Function for BC	71
	Bibliography	72

List of Figures

1.1	The Reynolds experiment; (a) laminar flow, (b) early transitional flow, and (c) turbulent flow.	8
1.2	Drawings of reference nozzle SMC000	17
1.3	Computational Domain	18
1.4	Computational grid of the entire domain	21
1.5	Computational grid in proximity of the nozzle	21
1.6	Convergence Analysis - Residuals	23
1.7	Convergence Analysis - Eddy Viscosity Contour	24
1.8	Result Contours - Axial Velocity	24
1.9	Result Contours - Density	24
1.10	Result Contours - Static Pressure	24
1.11	Result Contours - Turbulent Kinetic Energy	25
1.12	Result Contours - Specific Dissipation Rate	25
1.13	Comparison between computational grids - Mach number . .	26
1.14	Comparison between computational grids - Static Pressure .	27
1.15	Comparison between computational grids - Density	27
1.16	Comparison between computational grids - Turbulent Kinetic Energy	28
1.17	Comparison between computational grids - Specific Dissipation Rate	28
1.18	Comparison with reference data of Miller ¹⁰ - Axial Velocity .	29
1.19	Comparison with reference data of Miller ¹⁰ - Density	30
1.20	Comparison with reference data of Miller ¹⁰ - Static Pressure	30
1.21	Comparison with reference data of Miller ¹⁰ - Turbulent Kinetic Energy	30
1.22	Comparison with reference data of Miller ¹⁰ - Specific Dissipation Rate	30
1.23	Comparison with reference data of Miller ¹⁰ - Plot along $y = 0$ - Axial Velocity	31

1.24	Comparison with reference data of Miller ¹⁰ - Plot along $y = 0$	
	- Axial Velocity - Deep View	31
1.25	Comparison with reference data of Miller ¹⁰ - Plot along $y = 0$	
	- Density	32
1.26	Comparison with reference data of Miller ¹⁰ - Plot along $y = 0$	
	- Density - Deep View	32
1.27	Comparison with reference data of Miller ¹⁰ - Plot along $y = 0$	
	- Static Pressure	33
1.28	Comparison with reference data of Miller ¹⁰ - Plot along $y = 0$	
	- Static Pressure - Deep View	33
1.29	Comparison with reference data of Miller ¹⁰ - Plot along $y = 0$	
	- Turbulent Kinetic Energy	34
1.30	Comparison with reference data of Miller ¹⁰ - Plot along $y = 0$	
	- Specific Dissipation Rate	34
1.31	Comparison with reference data of Miller ¹⁰ - Plot along $x =$	
	0.03 - Axial Velocity	35
1.32	Comparison with reference data of Miller ¹⁰ - Plot along $x =$	
	0.03 - Density	35
1.33	Comparison with reference data of Miller ¹⁰ - Plot along $x =$	
	0.03 - Static Pressure	36
1.34	Comparison with reference data of Miller ¹⁰ - Plot along $x =$	
	0.03 - Turbulent Kinetic Energy	36
1.35	Comparison with reference data of Miller ¹⁰ - Plot along $x =$	
	0.03 - Specific Dissipation Rate	37
2.1	Phase delay due to the η distance between the two source points	45
2.2	Definition of θ , the polar angle	51
2.3	Definition of Ψ , the supplementary angle of θ	51
2.4	Correction factor of integral length scale due to Strouhal number	53
3.1	SMC0003 case - $ \tilde{p}_s $ Magnitude of the discrete Fourier trans-	
	form of shock pressure strength	57
3.2	Influence of $k_{1_{max}}$ on the final result for $\Psi = 70^\circ$	58
3.3	Case SMC0003 - Comparison of predictions with experiment ¹	
	of the SMC000 convergent nozzle operating at $Mj = 1.47$	
	and $TTR = 1.00$ at a distance of $R/D = 100$ and angles Ψ .	61

- 3.4 Case SMC0004 - Comparison of predictions with experiment¹
of the SMC000 convergent nozzle operating at $Mj = 1.00$
and $TTR = 2.70$ at a distance of $R/D = 100$ and angles Ψ . 62
- 3.5 Case SMC0008 - Comparison of predictions with experiment¹
of the SMC000 convergent nozzle operating at $Mj = 1.24$
and $TTR = 3.20$ at a distance of $R/D = 100$ and angles Ψ . 63

Nomenclature

Acronyms

BBSAN	Broad-Band Shock-Associated Noise
BC	Boundary Conditions
CFD	Computational Fluid Dynamics
CFL	Courant–Friedrichs–Lewy Number
CM	Control Mass
CV	Control Volume
DFT	Discrete Fourier Transform
DNS	Direct Numerical Simulation
FANS	Favre-Average Navier-Stokes
FT	Fourier Transform
FVM	Finite Volume Method
IDFT	Inverse Discrete Fourier Transform
IFT	Inverse Fourier Transform
LEE	Linearized Euler Equations
N-S	Navier-Stokes
NPR	Nozzle Pressure Ratio
PDE	Partial Differential Equation
RANS	Reynolds-Average Navier-Stokes

SDR Specific Dissipation Rate

SPL Sound Pressure Level

SST Shear Stress Transport

TKE Turbulent Kinetic Energy

TTR Total Temperature Ratio

Characteristic Numbers

Pr Prandtl Number

Re Reynolds Number

St Strouhal Number

Mathematical Operators

$\delta()$ Dirac Delta Function

δ_{ij} Kronecker Delta Function

$\frac{\partial}{\partial t}$ Temporal Partial Derivative

$\frac{\partial}{\partial x_i}$ Spatial Partial Derivative

$\nabla()$ Gradient Operator

$\nabla \cdot$ Divergence Operator

∇^2 Laplacian Operator

L_x Generic Linear Differential Operator

Physical Constants

γ Ratio of Specific Heats

C_p Specific Heat for Constant Pressure

C_V Specific Heat for Constant Volume

R Gas Constant

Symbols

η Distance Between Source Points

\mathbf{I}	Identity Tensor
\mathbf{n}	Normal Vector of the Boundary
\mathbf{q}	Heat Flux
\mathbf{T}	Stress Tensor
\mathbf{u}	Velocity Vector
\mathbf{x}	Observer Position
\mathbf{y}	Source Location
α	Thermal Diffusivity
β	Off-Design Parameter
μ	Dynamic Viscosity
μ_t	Eddy Viscosity
ν	Momentum Diffusivity
ν_t	Kinematic Eddy Viscosity
Ω	The Entire Volume of the CV
ω	Angular Frequency
ω	Specific Dissipation Rate of Turbulent Kinetic Energy
$\partial\Omega$	The Boundary of the CV
Φ	Generic Extensive Quantity
ϕ	Generic Intensive Quantity
π	Non-dimensional Pressure
π_g^n	n-th Component of the Vector Green's Function
Ψ	Potential Energy
ρ	Density
τ	Source Emission Time
τ_s	Integral Time Scale

τ_w	Wall Shear Stress
ε	Dissipation Rate of Turbulent Kinetic Energy
v	Module of Velocity Vector
a	Speed of Sound
E	Total Energy
e	Internal Energy
I	Turbulence Intensity
k	Turbulent Kinetic Energy
l_i	Integral Length Scale Component
M_d	Design Mach Number
M_j	Fully Expanded Mach Number
p	Static Pressure
T	Temperature
t	Time Variable
u_i	i-th Component of the Velocity Vector
u_s	Integral Velocity Scale
V	Volume
y^+	Wall y-plus

Abstract

In recent years, acoustic analogies have been proposed as a powerful tool to predict and describe how flow induces noise. Hence, this thesis aims to replicate the work of Miller¹⁰ in order to develop a software capable of evaluating jet noise caused by nozzles. The work is based on the papers created over the years by Tam and Auriault²³, Morris and Farassat¹³, Morris and Boluriaan¹², Proudman¹⁸, Morris and Miller¹⁴, Miller and Morris¹¹. The work is being done with a view to the future in which several improvements could be made. Another aspect is to summarize and revise all old papers by creating a reference work that can be useful to those who want to approach the world of aeroacoustics.

This work deals with a method to predict jet noise due to turbulent structures (mixing noise) and shock-wave shear-layer interactions (broad-band shock-associated noise). Discrete components (screeches) of shock-associated noise are not considered, while no assumptions are made regarding fine- or large-scale turbulent noise sources, self- or shear-noise, or convective amplification. The acoustic analogy is based on linearized Euler equations (LEE) and separates the sources from propagation. It is fed by a steady RANS solution with a closure model for turbulence based on Menter's $k - \omega$ SST model⁹. The main field variables and the turbulent ' k ' and ' ω ' quantities represent the input of the acoustic solver and allow to work out the integral scales of turbulence and source terms. The propagation is taken into account by evaluating a simplified vector Green's function linked to the inhomogeneous Helmholtz equation. Source terms, combined with Green's functions, allow to estimate the spectral density. Finally, some cases are analyzed and predictions are compared with experiments published in the open literature to validate the acoustic solver. It is generally captured the scaling of both mixing noise and BBSAN but there are some discrepancies due to the accuracy of the steady RANS turbulence model closure, the equivalent sources, and the use of a simplified vector Green's function.

Synopsis of the thesis

This thesis is structured in three chapters and some appendices. A brief overview of them is given here.

Chapter 1

An introduction to fluid dynamics is provided. The RANS approach and the $k - \omega$ SST closure model used to describe turbulent problems are outlined. Nozzle geometry and fluid dynamics test case is developed. The grid mesh generation and a grid convergence study are depicted. Finally, simulation results are shown and compared with reference data.

Chapter 2

The acoustic analogy based on the linearized Euler's equations is presented. The evaluation of the turbulent integral scales and the assumptions made to write the mixing noise and BBSAN source terms are explained.

Chapter 3

Some acoustic test cases are replicated and they are compared with experiments published in the open literature.

Appendices

An overview of the Green's function approach and the evaluation of Green's function of the inhomogeneous Helmholtz equation is presented. A section with all the necessary steps for plotting acoustic results is also added.

Introduction

In his final contribution to acoustics, Euler⁴ was surprised by the science he significantly contributed to.

“The most sublime research that Geometrist have undertaken nowadays with success is unarguably in all respect that of sound propagation. Because a given perturbation of air is dealt, this research has been all the more difficult, for among all those that were concerned with the movement of different bodies, none was found successful in describing the movement of air; so that this area of Mechanics was hitherto entirely unknown”...

...“When I investigated this topic for the first time, my main concern was to determine the speed at which a tremor is transmitted through the air; but now I will endeavor to detail all the particularities that may occur in the perturbation of air, and also the way they are altered in their propagation. This research is all the more interesting, that it is from there that all the variations that we observe in the sounds result”

As a matter of fact, Euler’s equations³, which describe the conservation of momentum in fluids, was the stepping stone on which all later developments of sound propagation would be based.

This golden age of acoustics is prior to the French revolution and can only be compared with the breakthroughs of the second half of the twentieth century. Indeed, although Euler⁴ successfully addresses acoustic propagation back in 1767, it is only in 1952 that Lighthill⁸ introduced the framework to apprehend the flow-noise generation mechanisms.

Neglecting the effect of viscosity, Lighthill⁸ recast Euler’s equations with the help of the continuity equation into the following equivalent formula,

$$\frac{\partial^2 \rho}{\partial t^2} - a^2 \nabla^2 \rho = \nabla \cdot \nabla \cdot (\rho \mathbf{u} \mathbf{u}) + \nabla^2 p - a^2 \nabla^2 \rho \quad (1)$$

where ρ is the density, \mathbf{u} is the velocity vector, p is the pressure and a is the speed of sound. On the left-hand side the wave operator, used to evaluate for the fluid particle displacement, is retrieved for the density. The right-hand side represents an equivalent source term for the wave equation. From now, for the first time, the amount of energy converted from the fluid motion into acoustics could be quantified by integrating the equation (1).

Powell¹⁷ in 1964, interpreting Lighthill's equation⁸, showed that the mechanisms of energy conversion are substantial only in the region of space where eddies are distorted. Out of this domain, the source term vanishes, and the perturbations in the fluid obey the simpler linear acoustic equation.

Although some recent acoustic analogies do not split the space between aerodynamic and acoustic driven regions, this separation is often used in aeroacoustics and distinguishes sound generation from its propagation. Yet, to achieve acoustic predictions with Lighthill's formula, a variable decomposition is furthermore required in order to dissociate the source term from the acoustic variable. This split is tedious in the source region, because there does not exist a general way to define acoustic perturbations. In fact, acoustics is a manner for energy to propagate without transporting matter. It must be recognized, that the conceptual framework of aeroacoustics raises in itself unresolved practical and fundamental questions.

In general, the compressible Navier-Stokes equations describe both the flow field, and the aerodynamically generated acoustic field. Thus, both may be solved for directly. This approach is called direct numerical simulation (DNS). Unfortunately, DNS requires very high numerical resolution due to the large differences in the length scale present between the acoustic variables and the flow variables. It is computationally very demanding and DNS has found its way only into Low-Re flows, like blood and flow near hearts. The advantageous approach splits the computational domain into different regions, such that the governing acoustic or flow field can be solved with different equations and numerical techniques. This would involve using two different numerical solvers, first a dedicated computational fluid dynamics tool and secondly an acoustic solver. The flow field is used to calculate the acoustical sources. These sources are provided to the second solver which calculates the propagation of acoustic waves.

Aeronautics had been the primary field of application for this theory; it was developed to identify the sound generation mechanisms in jets exhausting from turbofan engines and made noise reduction possible.

This acoustic analogy successfully predicted a remarkable scaling law for

the acoustic power radiated from jets. The increasing demand for quieter aircraft and the prodigious development in available computational resources led to a better understanding of the noise generation mechanisms.

Besides that, acoustic analogies were used combined with timely statistical simulations of the flow, to carry out jet noise predictions. Indeed, during the manufacturing processes of aircraft engines, accurate prediction tools were used to further reduce jet noise. In this view, there is a need for jet noise statistical modeling to properly assess the refraction effects encountered in the jets as well as the effects on the acoustic propagation of the turbofan installation under the wing plane. For such jet noise statistical modeling, acoustic propagation effects can be accounted for from an adjoint perspective and the use of the adjoint method to this end is now standard.

Chapter 1

Computational Fluid Dynamics

Computational fluid dynamics (CFD) is a branch of fluid mechanics that uses numerical analysis and data structures to analyze and solve problems that involve fluid flows. Computers are used to perform the calculations required to simulate the free-stream flow of the fluid and the interaction of the fluid (liquids and gases) with surfaces defined by boundary conditions. CFD is applied to a wide range of research and engineering problems in many fields of study. In this work it is applied to evaluate the flow field generated by a nozzle in particular operating conditions.

In recent years, CFD simulations proved to be an efficient way of solving and predicting fluid motion. It has the ability to capture key properties of the fluid (pressure, temperature, fluid dynamics characteristics). These types of simulations are performed thanks to software, which are programmed into solving, numerically, ‘Navier-Stokes’ equations (non-linear partial differential equations, PDEs) and the other closures and additional equations in a virtual discretized calculation domain.

The main steps for setting up a CFD simulation are listed below:

- Create the geometric model
- Create the best possible mesh for the model in agreement with the type of simulation that will be performed
- Choose the best mathematical models that will approximate the real problem
- Set up all fluid properties and the boundary conditions in the domain
- Choose the best mathematical methods to discretize model’s equations accordingly with the type of simulation that has to be performed

The accuracy of the final result is direct linked to all these steps. Commercial CFD software are developed to be robust and they give a solution even if a wrong condition or a parameter is set. That is why it is important to be able to have a critical view upon these results and to know which of the previous steps have to be modified in order to obtain an accurate model. It is obvious that, being the CFD software based on mathematical models, errors will be present in each resolution of the equations. In this way, the results from every simulation will be affected by numerical errors that do not depend on the model itself, but they are related to the mathematical models. To reduce skepticism about the solution, it is useful to initially replicate a similar test case whose solution is known. After the comparison with reference data and having proven a good result, it is reasonable to think that the same instruments and operator can achieve a good solution in a similar case. Other cautions to be taken are to check the graph of residuals and to check whether the mean flow quantities have a reasonable evolution. It is also essential to perform a grid convergence study that ensures that the grid is fine enough to adequately describe the problem it is intended to investigate.

In this work, the purpose of the CFD simulations is to quantify source terms in order to evaluate the sound pressure level (SPL) caused by the jet flow in different operating conditions. The fluid flow is studied within a certain region of space, commonly called Control Volume. The usual approach is to deal primarily with three quantities: mass, momentum and energy conservation.

The conservation laws describe the rate of change of a certain extended quantity within a particular control volume. A way to derive these conservation laws is starting from Reynolds' transport theorem.

These equations are non-linear, coupled, and difficult to solve. It is arduous to prove by the existing mathematical tools that a unique solution exists for particular boundary conditions.

1.1 Navier-Stokes Equations

This section deals with governing equations of fluid dynamics.

Thanks to Reynolds transport theorem, it is possible to link the rate of change of a certain extensive quantity in a control mass (CM) to the rate of change of the same quantity in a control volume (CV):

$$\frac{d\Phi}{dt} = \frac{\partial}{\partial t} \int_{\Omega} \rho \phi dV + \int_{\partial\Omega} \rho \phi \mathbf{u} \cdot \mathbf{n} dS \quad (1.1)$$

where $\Phi = \Phi(t)$ is the extensive quantity considered, $\phi = \phi(\mathbf{x}, t)$ is the relative intensive one, $\rho = \rho(\mathbf{x}, t)$ is the density, $\mathbf{u} = \mathbf{u}(\mathbf{x}, t)$ is the velocity vector, $\mathbf{n} = \mathbf{n}(\mathbf{x}, t)$ is the normal to the boundary of the control volume, \mathbf{x} is the generic location in the control volume and t is the time.

In that way it is possible to switch from a Lagrangian to a Eulerian approach. The latter is the most used in fluid mechanics where the focus is on a fixed control volume and it is important to know how flow variables change in each point of it.

Fluid flow equations are non-linear partial differential equations, which represent the correlation between the flow variables and their evolution in time and in space. The basic physical laws of motion that govern solids are valid also for gasses and liquids. The main difference is that fluids distort continuously without limit and during an analysis this characteristic must be taken into account.

In the following subparagraph three main equations which stand at the base of every CFD code are analyzed.

1.1.1 Mass Conservation Equation

The mass conservation equation is also known as the continuity equation. In a control mass, the mass does not change over time. According to this, applying Reynolds Transport theorem, and putting the attention on a control volume, the following equation can be written:

$$\frac{\partial}{\partial t} \int_{\Omega} \rho dV + \int_{\partial\Omega} \rho \mathbf{u} \cdot \mathbf{n} dS = 0 \quad (1.2)$$

where Ω is the control volume and $\partial\Omega$ is the boundary of the control volume. The equation (1.2) expresses that the mass in a control volume (first term)

can only change due to a mass flux through the surfaces of the control volume (second term).

1.1.2 Momentum Conservation Equation

The momentum is a vector defined as the product between velocity and mass. In that case, the physic law to respect is the second Newton's laws of motion. Following the same approach used for the mass conservation, the momentum equation can be written in an integral form as follow:

$$\frac{\partial}{\partial t} \int_{\Omega} \rho \mathbf{u} dV + \int_{\partial\Omega} \rho \mathbf{u} \mathbf{u} \cdot \mathbf{n} dS = \sum_k \mathbf{f}_k \quad (1.3)$$

The first term on the left hand side of equation (1.3) is the rate of change of the momentum in the control volume.

The second term represents the momentum convective transport through the boundary of the control volume.

The term on the right hand side represents the sum of all the external forces acting on the control volume. As always, forces can be divided into two categories:

- body forces: gravitational forces, Coriolis forces, electromagnetic forces, etc.
- surface forces: pressure and external forces.

If the forces acting on the fluid in control volume are not function of the system variables, they do not allow closure for the equations, so the flow can not be resolved. In this case, it is possible to make assumptions in order to model that terms as a function of system variables.

The most common assumption used is that of Newtonian fluids, which means assuming that the fluids obey to Newton's law of viscosity. Thus, the stress tensor \mathbf{T} of surface forces can be written as a sum of normal stresses, pressure tensor, and shear tensor.

$$\mathbf{T} = \left[-p + \left(\lambda + \frac{2}{3}\mu \right) \nabla \cdot \mathbf{u} \right] \mathbf{I} + 2\mu \mathbf{D}_0 \quad (1.4)$$

where $\mathbf{D}_0 = \frac{1}{2}(\nabla \mathbf{u} + \nabla \mathbf{u}^T) - \frac{1}{3}(\nabla \cdot \mathbf{u})\mathbf{I}$.

Furthermore, for Newtonian fluids, the bulk viscosity ' $\kappa = \lambda + \frac{2}{3}\mu$ ' is equal to zero according to Stokes' postulate.

Finally, the momentum equation can be expressed in the most familiar integral form:

$$\frac{\partial}{\partial t} \int_{\Omega} \rho \mathbf{u} dV + \int_{\partial\Omega} \rho \mathbf{u} \mathbf{u} \cdot \mathbf{n} dS = \int_{\partial\Omega} \mathbf{T} \cdot \mathbf{n} dS + \int_{\Omega} \rho \mathbf{b} dV \quad (1.5)$$

1.1.3 Energy Conservation Equation

This equation generally expresses the conservation of the total energy (sum of kinetic, internal and potential energy). In most common aerodynamic application, the influence of potential energy is usually neglected.

$$E = e + \frac{v^2}{2} + \Psi \simeq e + \frac{v^2}{2}$$

where $v = |\mathbf{u}| = \sqrt{u_i u_i}$ is the module of the velocity, e is the internal energy, Ψ is the potential energy.

Using the expression (1.1) and replacing $\phi = E$ it will follow:

$$\frac{\partial}{\partial t} \int_{\Omega} \rho E dV + \int_{\partial\Omega} \rho E \mathbf{u} \cdot \mathbf{n} dS = \sum_k E_k \quad (1.6)$$

with the contributions acting through the boundary of the control volume expressed by:

$$\sum_k E_k = \int_{\partial\Omega} (\mathbf{u} \cdot \mathbf{T}) \cdot \mathbf{n} dS - \int_{\partial\Omega} \mathbf{q} \cdot \mathbf{n} dS \quad (1.7)$$

where \mathbf{q} is the heat flux between the control volume and the environment. The first term on the right hand side of the equation (1.7) is the mechanical work per unit of time exchanged with the environment. It has got a reversible part linked to the isotropic part of the stress tensor \mathbf{T} and an irreversible part associated to the deviatoric part of \mathbf{T} .

The second term represents the heat transfer per unit time between the system and the environment. It is a diffusive flux of total energy always associated with entropy production, therefore it generates an irreversible transformation.

Here too, like in the momentum equation, the heat flux term \mathbf{q} is not function of the system variables so it must be modeled thanks to the Fourier's law:

$$\mathbf{q} = -\lambda \nabla T$$

where λ is the thermal conductivity coefficient.

The energy equation can be expressed in the integral form as follow:

$$\frac{\partial}{\partial t} \int_{\Omega} \rho E dV + \int_{\partial\Omega} \rho \left(E + \frac{p}{\rho} \right) \mathbf{u} \cdot \mathbf{n} dS = \int_{\partial\Omega} \mathbf{u} \cdot (2\mu \mathbf{D}_0) \cdot \mathbf{n} dS + \int_{\partial\Omega} \lambda \nabla T \cdot \mathbf{n} dS \quad (1.8)$$

1.1.4 Ideal Gas and Sutherland Law

It has been proven that Navier-Stokes equations are able to describe Newtonian flows. Some quantities must be expressed in a different way to have only six unknown variables (ρ, u, v, w, p, T) . The expression for internal energy (e) and the relation between specific heat for constant pressure (C_p) and volume (C_V) are described below:

$$e = C_V T; \quad \gamma \equiv \frac{C_p}{C_V}; \quad R = C_p - C_V \quad (1.9)$$

where R is the gas constant.

Only five equations were written so a sixth equation must be introduced to close the system. For common application the ideal gas law is often used:

$$p = \rho R T \quad (1.10)$$

where p is the pressure, ρ is the density, T is the temperature.

Moreover, the value of dynamic viscosity μ changes with temperature according to Sutherland Law:

$$\mu = \mu_0 \left(\frac{T}{T_0} \right)^{1.5} \frac{T_0 + S_\mu}{T + S_\mu} \quad (1.11)$$

where, for air, the constants are:

$$\mu_0 = 1.716 \cdot 10^{-5} \text{ N s m}^{-2}; \quad T_0 = 273 \text{ K}; \quad S_\mu = 111 \text{ K} \quad (1.12)$$

The thermal conductivity (λ) changes with the temperature too. It is common to evaluate this parameter from μ and Prandtl number, which express the ratio between momentum diffusivity and thermal diffusivity:

$$Pr \equiv \frac{\nu}{\alpha} = \frac{\mu/\rho}{\lambda/(C_p \rho)} = \frac{C_p \mu}{\lambda} \quad (1.13)$$

1.2 Turbulence

The understanding of turbulent behavior in flowing fluids is one of the most important problems in all of classical physics. It is a matter of fact that most fluid flows are turbulent and in many cases represent the dominant physics on all macroscopic scales throughout the known universe: from the interior of biological cells, to circulatory and respiratory systems of living creatures, to countless technological devices and household appliances of modern society, to geophysical and astrophysical phenomena including planetary interiors, oceans and atmospheres and stellar physics, and finally to galactic and even super galactic scales.

Despite the widespread occurrence of fluid flow, the ‘problem of turbulence’ remains to this day the last unsolved problem of classical mathematical physics. The problem of turbulence has been studied by many of the greatest physicists and engineers of the 19th and 20th Centuries, and yet we do not understand in complete detail how or why turbulence occurs, nor can we predict turbulent behavior with any degree of reliability, even in very simple flow situations.

The astounding polymath Leonardo Da Vinci was the first to study turbulence in 16th Century. Only hundred years later, in 1883, Osborne Reynolds¹⁹ systematically investigate the transition from laminar to turbulent flow by injecting a dye streak into flow through a pipe having smooth transparent walls. His observations led to identification of a single dimensionless parameter, now called the Reynolds number, and denoted by:

$$Re \equiv \frac{\rho v L}{\mu}$$

that completely characterizes flow behavior in this situation. In the expression ρ and μ are, respectively, the fluid properties density and dynamic viscosity. v is a velocity scale, and L is a characteristic length scale.

Reynolds number expresses the relative importance of inertial and viscous forces. Figure 1.1 provides a sketch of three flow regimes identified in the Reynolds experiments as Re is varied.

In Figure 1.1(a) laminar flow corresponding to $Re < 2000$ is depicted, for which dye injected into the stream can mix with the main flow of water only via molecular diffusion. This process is generally very slow compared with flow speeds, so little mixing, and hence very little apparent spreading of the dye streak, takes place over the length of the tube containing the flowing

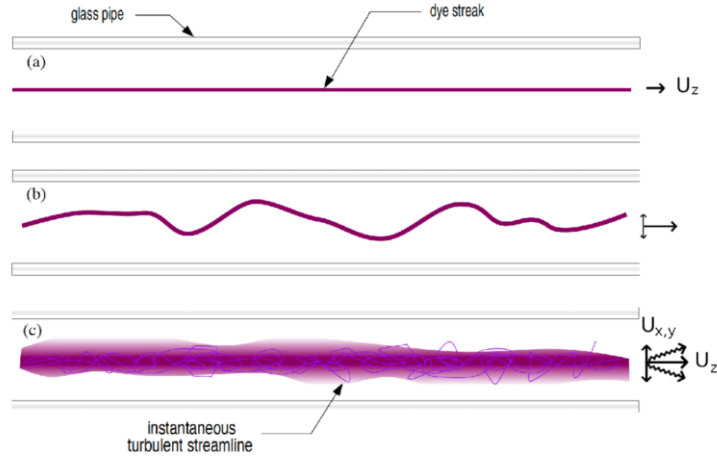


Figure 1.1: The Reynolds experiment; (a) laminar flow, (b) early transitional flow, and (c) turbulent flow.

water.

Figure 1.1(b) shows an early transitional state of flow ($2000 < Re < 2300$) for which the dye streak becomes wavy; but this flow is still laminar by the fact that the streak is still clearly identifiable with little mixing of dye and water having taken place.

Turbulent flow is indicated in Figure 1.1(c). Here, instantaneous streamlines change direction erratically, and the dye has mixed significantly with the water.

Important thing to note is that the enhanced mixing is a very important feature of turbulence and ultimately leads to the same end result as molecular diffusion, but on a much faster time scale.

Thus, turbulence is often said to ‘enhance diffusion’ and this viewpoint leads to a particular approach to modeling. Although the final result of turbulent mixing is the same as that of diffusive mixing, the physical mechanisms are very different. In fact, turbulence arises when molecular diffusion effects are actually quite small compared with those of macroscopic transport.

Clearly, if $\nu = \frac{\mu}{\rho}$ is small we should expect convective, non-linear behavior to be dominant, and this is the case in a turbulent flow.

In contrast, if ν is relatively large molecular diffusion will be dominant, and the flow will be laminar. In that way, non-linear and macroscopic transport case corresponding to turbulence occurs when the Reynolds number is large. This reflects the physical notion that mechanical energy injected into a fluid is generally on fairly large length and time scales, but this energy undergoes a ‘cascade’ whereby it is transferred to successively smaller scales

until it is finally dissipated (converted to thermal energy) on molecular scale (Kolmogorov⁷ scale).

This description underscores a second physical phenomenon associated with turbulence, the dissipation of kinetic energy. It is readily seen that there is not a precise characterization of turbulent flow in the sense of predicting, a priori, on the basis of specific flow conditions, when turbulence will or will not occur, or what would be its extent and intensity.

Due to the extremely complex nature of turbulence and its incomplete understanding, there is not a single accepted definition of turbulence. Many authors had tried to give a definition of turbulence but it is not unique. In the following passage, a precise definition of turbulence by G. T. Chapman and M. Tobak² is shown:

“Turbulence is any chaotic solution to the 3D Navier–Stokes equations that is sensitive to initial data and which occurs as a result of successive instabilities of laminar flows as a bifurcation parameter is increased through a succession of values.”

This definition contains specific elements that permit detailed examination of flow situations relating to turbulence. Firstly, it specifies equations (the Navier-Stokes Equations) whose solutions are to be associated with turbulence. Second, it requires that the fluid behavior be chaotic, but deterministic and not random. Third, turbulence must be three dimensional. This is consistent with the common classical viewpoint where generation of turbulence is ascribed to vortex stretching which can only occur in 3D.

The definition also imposes a requirement of ‘sensitivity to initial data’ which allows to distinguish highly irregular laminar motion from actual turbulence. A turbulent flow can be expected to exhibit some physical attributes:

- disorganized, chaotic, seemingly random behavior
- non repeatability (sensitivity to initial conditions)
- extremely large range of length and time scales
- enhanced diffusion (mixing) and dissipation
- three dimensional, time dependence and rotational
- intermittency in both space and time

1.3 Statistical Analysis and Modeling of Turbulence

Statistical analyses of turbulence have been used since the beginning of the studies. Hence, turbulent flows quantities are decomposed into their time-averaged and fluctuating components. According to this, Reynolds and Favre decomposition can be applied to Navier-Stokes Equations to obtain RANS (Reynolds Average Navier-Stokes) equations.

1.3.1 The RANS Equations

For most engineering applications, it is not possible to solve the instantaneous equations directly due to the enormous computational complexity required. At typical Reynolds numbers Navier-Stokes equations have very chaotic turbulent solutions and it is necessary to model the influence of smallest scales. Most turbulence models are based on one-point averaging of the instantaneous equations.

Let Φ be any dependent variable. It is convenient to define two different types of averaging of Φ :

- Classical time averaging (Reynolds averaging):

$$\overline{\Phi} \equiv \frac{1}{T^*} \int_0^{T^*} \Phi(t) dt \quad (1.14)$$

$$\Phi' \equiv \Phi - \overline{\Phi} \quad (1.15)$$

- Density weighted time averaging (Favre averaging):

$$\tilde{\Phi} \equiv \frac{\overline{\rho\Phi}}{\overline{\rho}} \quad (1.16)$$

$$\Phi'' \equiv \Phi - \tilde{\Phi} \quad (1.17)$$

With the above definitions it is important to note that $\overline{\Phi'} = 0$, but $\overline{\Phi''} \neq 0$. It is important to choose correctly the integration time T^* . It must be very large compared with the time scales of the fluctuations but short enough when compared with the timescales of mean-field fluctuations.

In order to obtain an averaged form of the governing equations, the instantaneous continuity equation (1.2), momentum equation (1.3) and energy equation (1.8), in their differential form, are time-averaged. Using the Einstein notation, the RANS equation in their compressible form are listed below:

$$\frac{\partial \bar{\rho}}{\partial t} + \frac{\partial}{\partial x_i} [\bar{\rho} \tilde{u}_i] = 0 \quad (1.18)$$

$$\frac{\partial}{\partial t} (\bar{\rho} \tilde{u}_i) + \frac{\partial}{\partial x_j} [\bar{\rho} \tilde{u}_i \tilde{u}_j + \bar{p} \delta_{ij} + \overline{\rho u_i'' u_j''} - \bar{\tau}_{ji}] = 0 \quad (1.19)$$

$$\frac{\partial}{\partial t} (\bar{\rho} \tilde{E}) + \frac{\partial}{\partial x_j} [\bar{\rho} \tilde{u}_j \tilde{E} + \tilde{u}_j \bar{p} + \overline{u_j'' p} + \overline{\rho u_j'' E''} + \bar{q}_j - \overline{u_i \tau_{ij}}] = 0 \quad (1.20)$$

In these expressions τ_{ij} is the generic component of the matrix $\boldsymbol{\tau} = 2\mu \mathbf{D}_0$. The different expression of \tilde{E} must be underlined.

$$\tilde{E} \equiv \tilde{e} + \frac{\tilde{u}_k \tilde{u}_k}{2} + k \quad (1.21)$$

In the equation (1.21) an additional term appears, k . It is the turbulent kinetic energy and is expressed in the following way:

$$k \equiv \frac{\widetilde{u_k'' u_k''}}{2} \quad (1.22)$$

1.3.2 Approximations and Modeling

Focusing on the set of partial differential equations (1.18)-(1.20), several unknown correlation terms are involved. In order to obtain a closed form of equations, it is necessary to model these unknowns. Analyzing equations (1.18)-(1.20), it is advantageous to rewrite some terms in the following way:

$$\overline{\tau_{ji}} = \widetilde{\tau_{ji}} + \overline{\tau_{ji}''} \quad (1.23)$$

$$\overline{u_j'' p} + \overline{\rho u_j'' E''} = C_p \overline{\rho u_j'' T} + u_i \overline{\rho u_i'' u_j''} + \frac{\overline{\rho u_j'' u_i'' u_i''}}{2} \quad (1.24)$$

$$\bar{q}_j = -C_p \frac{\mu}{Pr} \frac{\partial \bar{T}}{\partial x_j} = -C_p \frac{\mu}{Pr} \frac{\partial \tilde{T}}{\partial x_j} - C_p \frac{\mu}{Pr} \frac{\partial \overline{T''}}{\partial x_j} \quad (1.25)$$

$$\overline{u_i \tau_{ij}} = \widetilde{u_i \tau_{ij}} + \overline{u_i'' \tau_{ij}} + \widetilde{u_i} \overline{\tau_{ij}''} \quad (1.26)$$

Where the perfect gas relations (1.10) and Fourier's law have been used. Fluctuations in the molecular viscosity, μ , have been neglected. Substituting these relations into equations (1.18)-(1.20):

$$\frac{\partial \bar{\rho}}{\partial t} + \frac{\partial}{\partial x_i} [\bar{\rho} \widetilde{u_i}] = 0 \quad (1.27)$$

$$\frac{\partial}{\partial t} (\bar{\rho} \widetilde{u_i}) + \frac{\partial}{\partial x_j} \left[\bar{\rho} \widetilde{u_i u_j} + \bar{p} \delta_{ij} + \underbrace{\overline{\rho u_i'' u_j''}}_{(1^*)} - \widetilde{\tau_{ji}} - \underbrace{\overline{\tau_{ji}''}}_{(2^*)} \right] = 0 \quad (1.28)$$

$$\begin{aligned} \frac{\partial}{\partial t} (\bar{\rho} \widetilde{E}) + \frac{\partial}{\partial x_j} \left[\bar{\rho} \widetilde{u_j E} + \widetilde{u_j} \bar{P} + \underbrace{C_P \overline{\rho u_j'' T}}_{(3^*)} + \underbrace{\widetilde{u_j} \overline{\rho u_i'' u_j''}}_{(4^*)} + \underbrace{\frac{\overline{\rho u_j'' u_i'' u_i''}}{2}}_{(5^*)} \right. \\ \left. - C_P \frac{\mu}{Pr} \frac{\partial \widetilde{T}}{\partial x_j} - \underbrace{C_P \frac{\mu}{Pr} \frac{\partial \overline{T''}}{\partial x_j}}_{(6^*)} - \widetilde{u_i \tau_{ij}} - \underbrace{\overline{u_i'' \tau_{ij}}}_{(7^*)} - \underbrace{\widetilde{u_i} \overline{\tau_{ij}''}}_{(8^*)} \right] = 0 \end{aligned} \quad (1.29)$$

The terms marked, from (1*) to (8*), are unknowns and have to be modeled in some way. Term (1*) and (4*) can be modeled using an eddy-viscosity assumption for the Reynolds stresses, τ_{ij}^{turb} :

$$\tau_{ij}^{turb} \equiv -\overline{\rho u_i'' u_j''} \approx 2\mu_t \widetilde{S_{ij}^*} - \frac{2}{3} \bar{\rho} k \delta_{ij} \quad (1.30)$$

Where μ_t is a turbulent viscosity, which is estimated with a turbulence model. The last term is included in order to ensure that the trace of the Reynolds stress tensor is equal to $-2\rho k$, as it should be.

Term (3*), corresponding to turbulent transport of heat, can be modeled using a gradient approximation for the turbulent heat-flux:

$$q_j^{turb} \equiv C_p \overline{\rho u_j'' T} \approx -C_p \frac{\mu_t}{Pr_t} \frac{\partial \widetilde{T}}{\partial x_j} \quad (1.31)$$

Where Pr_t is a turbulent Prandtl number. Often a constant $Pr_t \approx 0.9$ is used.

The term (2*) and (8*) can be neglected if:

$$|\widetilde{\tau_{ij}}| \gg |\overline{\tau_{ij}''}| \quad (1.32)$$

this hypothesis is true for most common fluids.

Term (5*) and (7*), corresponding to turbulent transport and molecular diffusion of turbulent energy, can be neglected if the turbulent energy is small compared to the enthalpy:

$$k \ll \tilde{h} = C_p \tilde{T} \quad (1.33)$$

This is a reasonable approximation for most flows below the hyper-sonic regime.

Term (6*) is an artifact from the Favre averaging. It is related to heat conduction effects associated with temperature fluctuations. It can be neglected if:

$$\left| \frac{\partial^2 \tilde{T}}{\partial x_j^2} \right| \gg \left| \frac{\partial^2 \overline{T''}}{\partial x_j^2} \right| \quad (1.34)$$

This is true for virtually all flows, and has been assumed in all following equations.

1.3.3 Closed Approximated RANS Equations

All the governing equations (1.18)-(1.20), with the assumptions made in the previous paragraph, can be written as in (1.35)-(1.37). These equations are valid for a perfect gas and don't consider fluctuations in the molecular viscosity.

$$\frac{\partial \bar{\rho}}{\partial t} + \frac{\partial}{\partial x_i} [\bar{\rho} \tilde{u}_i] = 0 \quad (1.35)$$

$$\frac{\partial}{\partial t} (\bar{\rho} \tilde{u}_i) + \frac{\partial}{\partial x_j} [\bar{\rho} \tilde{u}_j \tilde{u}_i + \bar{p} \delta_{ij} - \widetilde{\tau_{ji}^{tot}}] = 0 \quad (1.36)$$

$$\frac{\partial}{\partial t} (\bar{\rho} \tilde{e}_0) + \frac{\partial}{\partial x_j} [\bar{\rho} \tilde{u}_j \tilde{e}_0 + \tilde{u}_j \bar{p} + \widetilde{q_j^{tot}} - \tilde{u}_i \widetilde{\tau_{ij}^{tot}}] = 0 \quad (1.37)$$

Where:

$$\widetilde{\tau_{ij}^{tot}} \equiv \widetilde{\tau_{ij}^{lam}} + \widetilde{\tau_{ij}^{turb}} \quad (1.38)$$

$$\widetilde{\tau_{ij}^{lam}} \equiv \widetilde{\tau_{ij}} = \mu \left(\frac{\partial \tilde{u}_i}{\partial x_j} + \frac{\partial \tilde{u}_j}{\partial x_i} - \frac{2}{3} \frac{\partial \tilde{u}_k}{\partial x_k} \delta_{ij} \right) \quad (1.39)$$

$$\widetilde{\tau_{ij}^{turb}} \equiv -\overline{\rho u_i'' u_j''} \approx \mu_t \left(\frac{\partial \widetilde{u}_i}{\partial x_j} + \frac{\partial \widetilde{u}_j}{\partial x_i} - \frac{2}{3} \frac{\partial \widetilde{u}_k}{\partial x_k} \delta_{ij} \right) - \frac{2}{3} \bar{\rho} k \delta_{ij} \quad (1.40)$$

$$\widetilde{q_j^{tot}} \equiv \widetilde{q_j^{lam}} + \widetilde{q_j^{turb}} \quad (1.41)$$

$$\widetilde{q_j^{lam}} \equiv \widetilde{q}_j \approx -C_p \frac{\mu}{Pr} \frac{\partial \widetilde{T}}{\partial x_j} = -\frac{\gamma}{\gamma - 1} \frac{\mu}{Pr} \frac{\partial}{\partial x_j} \left[\frac{\bar{p}}{\bar{\rho}} \right] \quad (1.42)$$

$$\widetilde{q_j^{turb}} \equiv C_p \overline{\rho u_j'' \widetilde{T}} \approx -C_p \frac{\mu_t}{Pr_t} \frac{\partial \widetilde{T}}{\partial x_j} = -\frac{\gamma}{\gamma - 1} \frac{\mu_t}{Pr_t} \frac{\partial}{\partial x_j} \left[\frac{\bar{p}}{\bar{\rho}} \right] \quad (1.43)$$

$$\bar{p} = (\gamma - 1) \bar{\rho} \left(\widetilde{e}_0 - \frac{\widetilde{u}_k \widetilde{u}_k}{2} - k \right) \quad (1.44)$$

Following this formulation, if a separate turbulence model is used to calculate μ_t , k and Pr_t , and gas data is given for μ , γ and Pr , these equations form a closed set of partial differential equations which can be solved numerically.

1.3.4 Turbulence Model: k - ω SST

The k - ω SST model is one of the most commonly used turbulence models. It is a two equation model, that means, it includes two extra transport equations to represent the turbulent properties of the flow. This allows a two equation model to account for history effects like convection and diffusion of turbulent energy.

The first transported variable is turbulent kinetic energy, k . The second one is the specific dissipation rate, ω . The latter is a variable that determines the scale of the turbulence, whereas the first quantity, k , determines the turbulence energy.

The Shear Stress Transport (SST) formulation⁹ combines the best of two worlds. The use of a k - ω formulation in the inner parts of the boundary layer makes the model directly usable all the way down to the wall through the viscous sub-layer, hence the SST k - ω model can be used as a Low-Re turbulence model without any extra damping functions. The SST formulation also switches to a k - ε behavior in the free-stream and, thereby, avoids the common k - ω problem that the model is too sensitive to the inlet free-stream turbulence properties. SST k - ω model often merit it for its good behavior in adverse pressure gradients and separating flow.

In the k - ω SST, the original k - ω has an additional cross-diffusion term

in the ω equation and the modeling constants are different. The original $k - \omega$ model is then multiplied by a function F_1 and the transformed model by a function $(1 - F_1)$, and both are added together.

The function F_1 is designed to be one in the near wall region (activating the original model) and zero away from the surfaces. The blending will take place in the wake region of the boundary layer. This function is expressed in the equation (1.45):

$$F_1 = \tanh \left\{ \left\{ \min \left[\max \left(\frac{\sqrt{k}}{\beta^* \omega y}, \frac{500\nu}{y^2 \omega} \right), \frac{4\sigma_{\omega 2} k}{CD_{k\omega} y^2} \right] \right\}^4 \right\} \quad (1.45)$$

where y is the distance to the next surface, β^* is a constant equal to 0.09 and the variable $CD_{k\omega}$ is:

$$CD_{k\omega} = \max \left(2\rho\sigma_{\omega 2} \frac{1}{\omega} \frac{\partial k}{\partial x_i} \frac{\partial \omega}{\partial x_i}, 10^{-20} \right) \quad (1.46)$$

The two transport equations, which represent the turbulent properties, are given here:

$$\frac{\partial k}{\partial t} + u_j \frac{\partial k}{\partial x_j} = P_k - \beta^* k \omega + \frac{\partial}{\partial x_j} \left[(\nu + \sigma_k \nu_T) \frac{\partial k}{\partial x_j} \right] \quad (1.47)$$

$$\begin{aligned} \frac{\partial \omega}{\partial t} + u_j \frac{\partial \omega}{\partial x_j} = \\ \alpha S^2 - \beta \omega^2 + \frac{\partial}{\partial x_j} \left[(\nu + \sigma_{\omega} \nu_T) \frac{\partial \omega}{\partial x_j} \right] + 2(1 - F_1) \sigma_{\omega 2} \frac{1}{\omega} \frac{\partial k}{\partial x_i} \frac{\partial \omega}{\partial x_i} \end{aligned} \quad (1.48)$$

Where S is the module of the mean rate-of-strain tensor (the absolute value of the vorticity), defined as:

$$S = \sqrt{2\mathbf{S} : \mathbf{S}} = \sqrt{2S_{ij}S_{ij}} \quad (1.49)$$

in which:

$$\mathbf{S} = \frac{1}{2} (\nabla \mathbf{u} + \nabla \mathbf{u}^T) \quad (1.50)$$

In this model the Kinematic Eddy Viscosity (ν_t) must be evaluated as follows:

$$\nu_T = \frac{a_1 k}{\max(a_1 \omega, SF_2)} \quad (1.51)$$

where $a_1 = 0.31$ and

$$F_2 = \tanh \left[\left[\max \left(\frac{2\sqrt{k}}{\beta^*\omega y}, \frac{500\nu}{y^2\omega} \right) \right]^2 \right] \quad (1.52)$$

The quantity P_k must be calculated too:

$$P_k = \min \left(\tau_{ij} \frac{\partial u_i}{\partial x_j}, 10k\omega\beta^* \right) \quad (1.53)$$

The generic constant of the model ϕ changes due to blending function F_1 according to this law:

$$\phi = \phi_1 F_1 + \phi_2 (1 - F_1) \quad (1.54)$$

where the subscript ‘1’ refers to constants of the original $k - \omega$ model; otherwise the subscript ‘2’ refers to constants of the $k - \varepsilon$.

The coefficients needed to close the model are:

$$\alpha_1 = \frac{5}{9}; \quad \alpha_2 = 0.44 \quad (1.55)$$

$$\beta_1 = 0.0750; \quad \beta_2 = 0.0828 \quad (1.56)$$

$$\sigma_{k1} = 0.85; \quad \sigma_{k2} = 1 \quad (1.57)$$

$$\sigma_{\omega1} = 0.5; \quad \sigma_{\omega2} = 0.856 \quad (1.58)$$

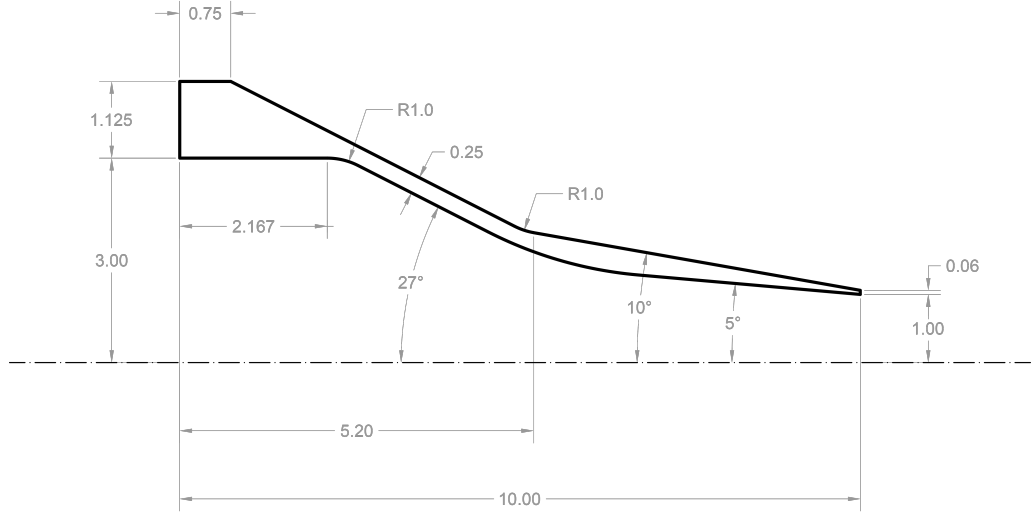


Figure 1.2: Drawings of reference nozzle SMC000

1.4 Fluid Dynamic Test Case

This section deals with a fluid dynamic test case in which a solution of a compressible flow through the nozzle is worked out. This is a case of under-expansion leading to shock-cell structures in the plume.

The SMC000 nozzle has been chosen so that results could be compared with experimental data available in open literature. Based on this, the simulation will be one of many that will be provided to the aeroacoustics solver. With an under-expanded case, both the contribution of mixing noise and broad-band shock associated noise can be evaluated.

1.4.1 Nozzle Geometry

The SMC000 geometry is replicated starting from the drawing of acoustic reference nozzle in the publication by Bridges and Brown¹.

This nozzle has a ratio $\frac{A_1}{A_2} = 9.0$, a length $L = 0.254$ m, an inlet diameter $D_1 = 0.1524$ m and a throat diameter $D_2 = 0.0508$ m. Where the subscript ‘1’ indicates the inlet section, otherwise the subscript ‘2’ is associated to the outlet section (throat section).

In the Figure 1.2 the convergent nozzle is sketched out. All distances are measured in inches but all lengths are later scaled according to the metric system.

In order to analyze the flow field outside the nozzle, it is necessary to create a domain which extends $100D_2$ downstream from the nozzle exit and $50D_2$ in the radial direction from the center line.

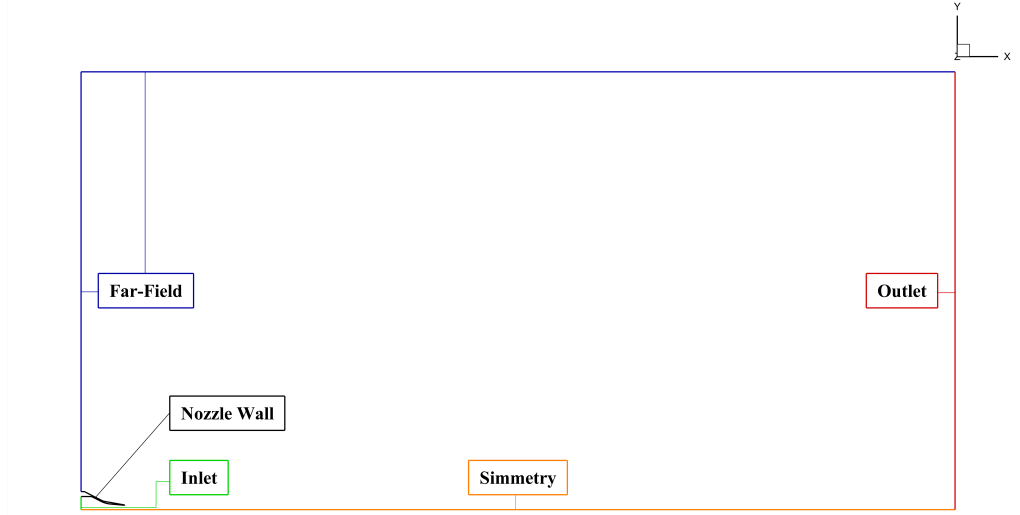


Figure 1.3: Computational Domain

It is an axisymmetric nozzles, hence, a single plane in the stream-wise and radial direction of the nozzle is considered. It contains the nozzle interior, exterior, and plume region. The exact axisymmetric geometry used in the aeroacoustics reference experiments is also accounted for. Only half model is replicated to save computational efforts.

Therefore, the final computational domain is represented in the Figure 1.3.

1.4.2 Operating Conditions

The test case analyzed has the following thermodynamic conditions:

$$M_d = 1.00; \quad M_j = 1.47; \quad TTR = 1.00 \quad (1.59)$$

where M_d is the design Mach number. It is equal to one because the nozzle has only a convergent part, so it indicates that the ideal Mach number in the throat section should be equal to one.

M_j in the fully expanded Mach number. Values greater than one represent conditions of under-expansion, while values less than one represent cases of over-expansion. If M_j is equal to one the nozzle is in an adapted condition. TTR is the total temperature ratio and expresses the ratio between the total temperature and the free-stream temperature.

With the definition of these three values it is possible to know all variables needed to define boundary conditions.

In a first approximation, discarding the effect of viscosity and considering an adiabatic nozzle, it is possible to derive an expression which relates the areas

of two cross sections of a flow pipe and the average Mach numbers over the same cross sections. If two section are considered, the inlet and the outlet of the nozzle, and keeping in mind that the Mach number in the throat section is equal to one, the inlet Mach number can be evaluated thanks to the next equation:

$$\frac{A_1}{A^*} = \frac{A_1}{A_2} = \frac{1}{M_1} \left(\frac{1 + \delta M_1^2}{1 + \delta} \right)^{\frac{\gamma+1}{2(\gamma-1)}} \quad (1.60)$$

where,

$$\delta = \frac{\gamma - 1}{2} \quad (1.61)$$

The fully expanded Mach number (M_j) is directly linked to the nozzle pressure ratio (NPR) which relates the total pressure to the free-stream pressure.

$$NPR = \frac{p_0}{p_\infty} = (1 + \delta M_j^2)^{\frac{\gamma}{\gamma-1}} \quad (1.62)$$

The same happens with the total temperature ratio:

$$TTR = \frac{T_0}{T_\infty} \quad (1.63)$$

According to these expressions it is easy to assess the total pressure and the total temperature in order to assign them as constants at the inlet boundary. Static quantities can be readily calculated from the inlet Mach number (M_1). Turbulence intensity (I) and turbulent viscosity ratio $\left(\frac{\mu_t}{\mu}\right)$ should be set as boundary conditions. Values are assigned in order to be the same as in the reference solution:

$$I = \sqrt{\frac{0.01\mu_0}{1.5}}; \quad \frac{\mu_t}{\mu} = 0.005\rho_0 \quad (1.64)$$

In the far-field, free-stream Mach number is set as ' $M_\infty = 0.01$ ' for stability and convergence. The other free-stream parameter are set equal to the ambient values:

$$p_\infty = 101\,325 \text{ Pa}; \quad T_\infty = 293.15 \text{ K} \quad (1.65)$$

At the outlet boundary a pressure equal to p_∞ is set. Moreover, the x axis is set as a symmetric axis. In conclusion, all nozzle surfaces are set as a wall boundary with no-slip condition and a heat flux equal to zero.

1.4.3 Fluid Dynamics Mesh Generation

Above all, it is necessary to consider the operating condition in order to generate a computational grid which will let the solver able to calculate flow quantities in the right way. This concept is the basis of the computational fluid dynamic. In fact, the grid could be refined enough in some zones and pretty course in others. The ability is in the definition of an optimized grid which is able to catch quantities variation but with as few nodes as possible to save computational efforts.

With this in mind, the spacing of the first cell near walls must be chosen in order to have $y^+ \simeq O(1)$, accordingly to the formula:

$$y^+ = \frac{y}{\nu} \sqrt{\frac{\tau_w}{\rho}} \quad (1.66)$$

where y is the absolute distance from the wall, ν is the kinematic viscosity, τ_w is the wall shear stress and ρ is the density.

Only in that case, it is possible to describe without ‘wall-function’ models the boundary layer, describing correctly the laminar sub-layer region where velocity profiles is assumed to be laminar and viscous stress dominates the wall shear.

After these considerations, a structured grid is created. Most nodes are located in the plume region and in the shear layer. An overview is represented in Figure 1.4.

A detailed view of the mesh in proximity of the nozzle is depicted in the Figure 1.5.

The grid is generated with the software ICEM CFD and there are about 330000 nodes. Spatial laws are chosen on the edges in order to have the right density of cells. Special emphasis is given to contiguous edges with the aim of maintaining the right spacing. This is important because having two adjacent cells which have a huge difference in dimension can lead to an inexact result.

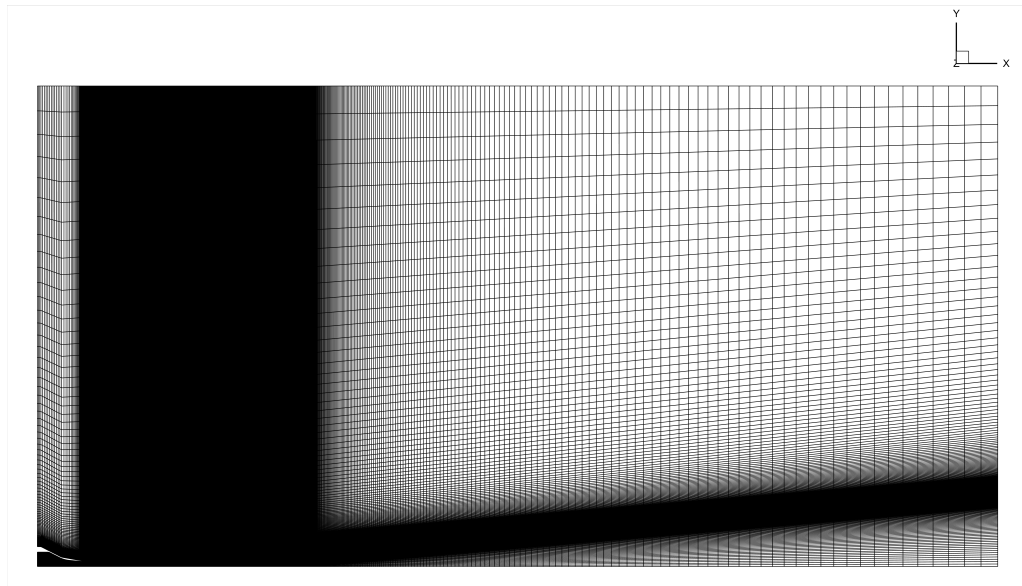


Figure 1.4: Computational grid of the entire domain

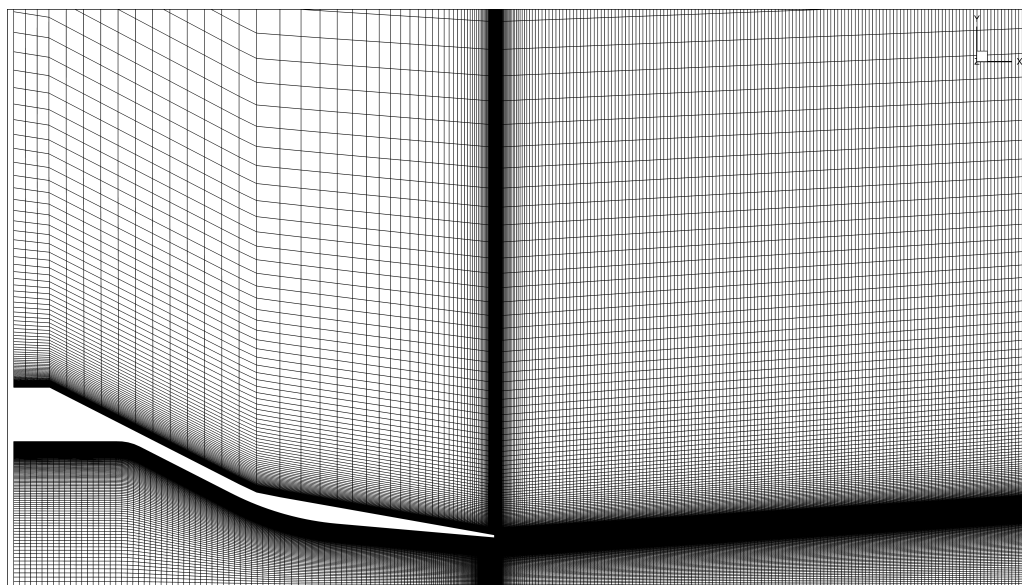


Figure 1.5: Computational grid in proximity of the nozzle

1.4.4 Results

In these section the solution is shown. Contour plot of the most relevant variables are generated with the post-processing software Tecplot360.

The steady RANS solution is found using the commercial software Ansys Fluent, which solves numerically the Navier-Stokes equations system and the other closure relations using a finite volume method (FVM) for discretization. In this work an axisymmetric nozzles is examined. Hence, 2D simulation with a single plane in the stream-wise and radial direction of the nozzle is carried out. Numerical solutions are governed by the steady RANS equations closed by the Menter SST⁹ turbulence model. Roe flux vector construction is used for spatial discretization and is second order accurate.

The flow field is initialized with an ‘Hybrid Initialization⁵’, which solves the Laplace equation to produce a velocity field that conforms to complex domain geometries, and a pressure field which smoothly connects high and low pressure values in the computational domain. All other variables will be patched based on domain averaged values.

Initial iterations use a Courant-Friedrichs-Lewy (CFL) number of 1.0 and increase to a CFL number of 100.0 with the ‘Solution-Steering’ method.

This technique is divided in two iterative stage:

- Stage 1: navigate the solution from the difficult initial phase of the solution toward convergence by insuring maximum stability. During this stage, the solution is advanced gradually from 1st-order accuracy to 2nd-order accuracy at a constant low CFL value.
- Stage 2: solution is driven hard towards convergence by regular adjustments of the CFL value to insure fast convergence as well as to prevent possible divergence. The residual history is monitored and analyzed through regular intervals to determine if an increase or decrease in CFL value is needed to obtain fast convergence or to prevent divergence.

To evaluate the convergence of the solution residuals, mass flow rate and eddy viscosity contour are analyzed. Firstly, in the Figure 1.6 residuals are plotted and it can be seen that each residual is stabilized. Some occasional large increases in residuals can be noted but they are linked to an abrupt variation of CFL in order to avoid divergence. Second, the mass flow rate is evaluated and it allows to estimate the flow rate error through the boundaries. Little values represent a better convergence and in the Table 1.1 the mass flow rate error is illustrated. Finally, the contour of eddy viscosity is depicted

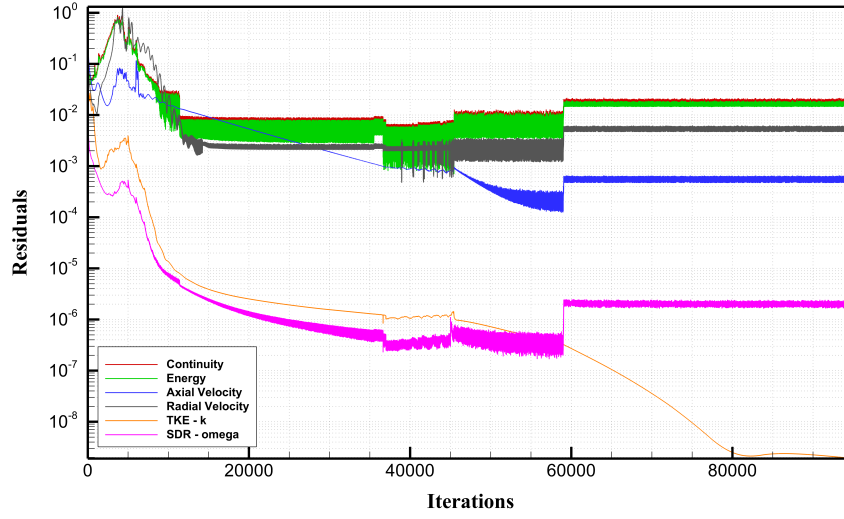


Figure 1.6: Convergence Analysis - Residuals

Mass Flow Rate	[kg/s]
Inlet	1.685340
Outlet1	83.925635
Outlet2	0.233272
Outlet3	-85.844296
Net	-0.000046

Table 1.1: Convergence Analysis - Mass Flow Rate

in the Figure 1.7 and it is checked that viscosity ratio values do not exceed $1 \cdot 10^5$, otherwise, in under-expanded jets, the solution under-predict Mach number peaks in the shock cells and the result is not good.

From Figure 1.8 to Figure 1.12 contours of axial velocity, density, static pressure, turbulent kinetic energy and specific dissipation rate are displayed. As expected, the pressure mismatch between the jet and the ambient air (under-expanded case) leads to the formation of (diamond-shaped) shock-cells as shown in Figure 1.8, which strongly interact with the turbulent structures developing in the mixing layer around the potential core.

The same pattern can be seen for density and static pressure, in Figure 1.10 and Figure 1.9 respectively.

The turbulent kinetic energy assumes relevant values in the shear layer as expected (Figure 1.11) and the dissipation of turbulent kinetic energy starts from wall where speed is set to zero for no-slip condition and continues in the shear layer (Figure 1.12).

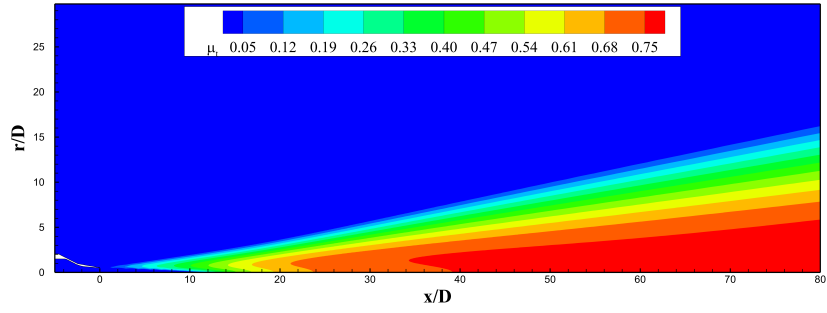


Figure 1.7: Convergence Analysis - Eddy Viscosity Contour

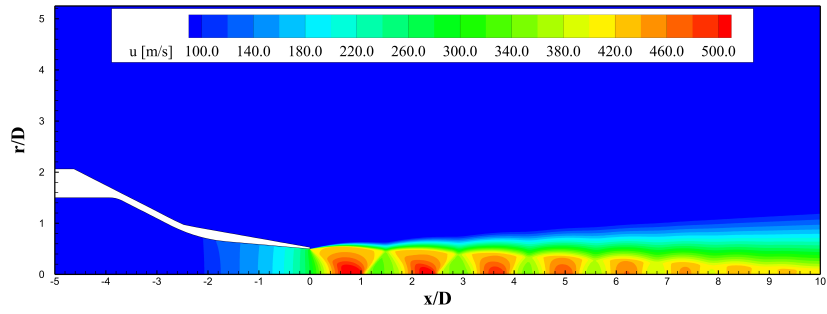


Figure 1.8: Result Contours - Axial Velocity

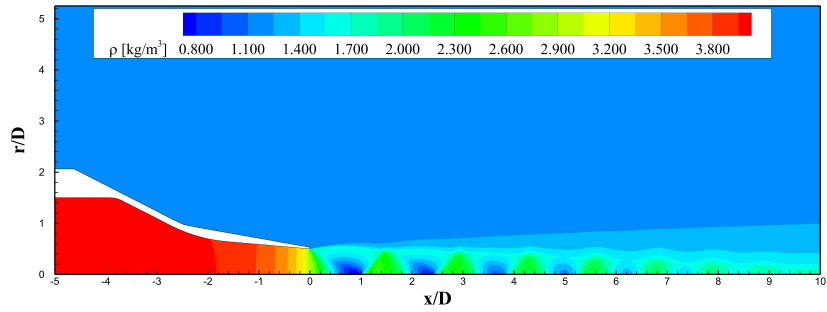


Figure 1.9: Result Contours - Density

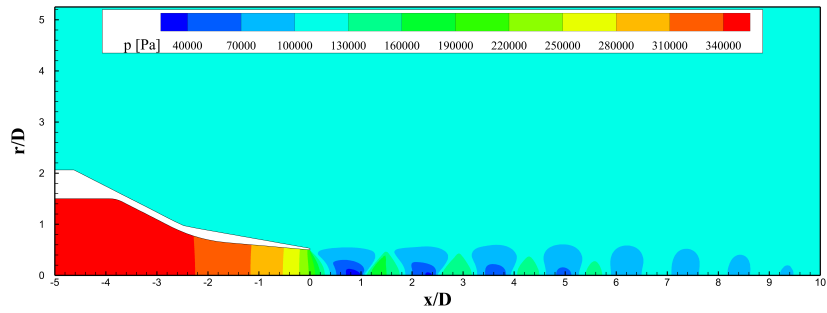


Figure 1.10: Result Contours - Static Pressure

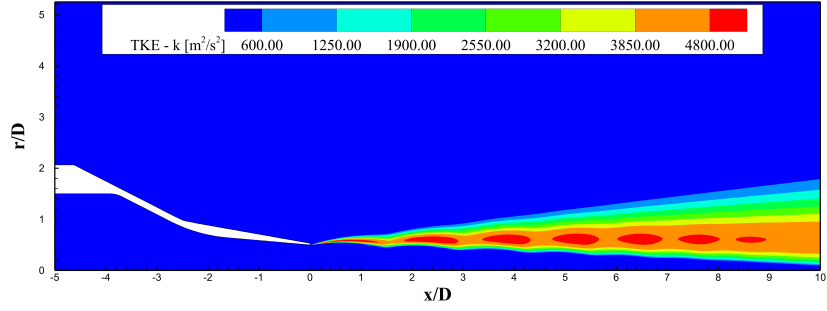


Figure 1.11: Result Contours - Turbulent Kinetic Energy

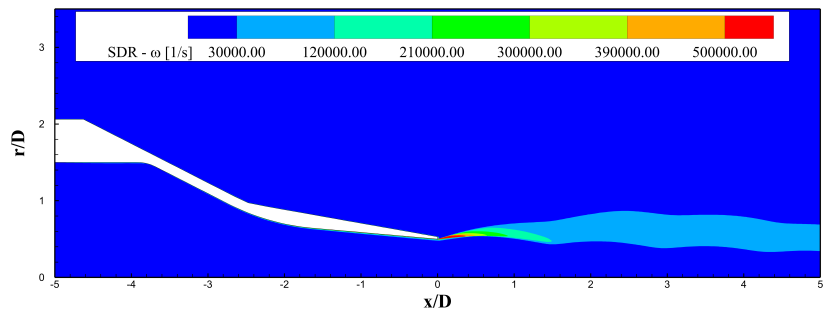


Figure 1.12: Result Contours - Specific Dissipation Rate

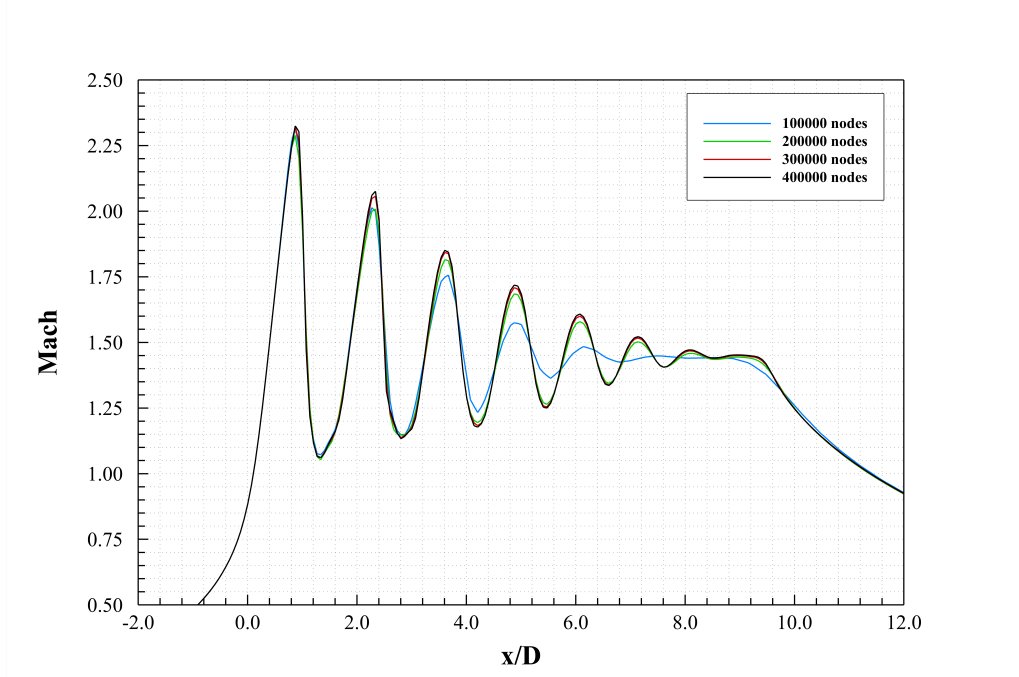


Figure 1.13: Comparison between computational grids - Mach number

1.4.5 Grid Convergence Study

The examination of the spatial convergence of a simulation is a straightforward method for determining the ordered discretization error in a CFD simulation and how well or poorly such a grid succeeds or fails in capturing certain physical quantities variation.

The approach provides the generation of grids with a finer grid spacing. In generating each fine computational grid, the number of nodes is proportionally increased on all edges. Subsequently, the same fluid dynamic simulation with the same boundary conditions (see paragraph 1.4.2) is done for each grid. In this under-expanded case, it is important to capture the evolution of the variables in the flow field due to the presence of shock-cell structures. Consequently, a comparison between primitive quantities is done. The attention has been focused on the symmetry line. In the following images 1.13-1.17 all compares are illustrated.

It is clear from these comparisons that the best choice is a computational grid which has about three thousand nodes because it is able to catch all peaks of the quantities along the plume and does not require a large amount of nodes. For this reason the grid used to evaluate results under these and other operating conditions is the one with almost 330000 nodes, represented in the section 1.4.3.

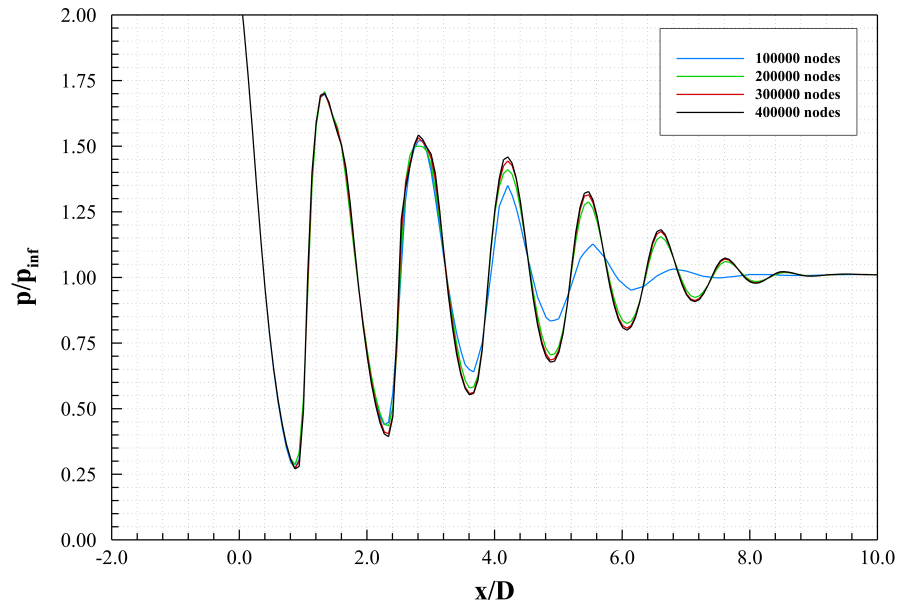


Figure 1.14: Comparison between computational grids - Static Pressure

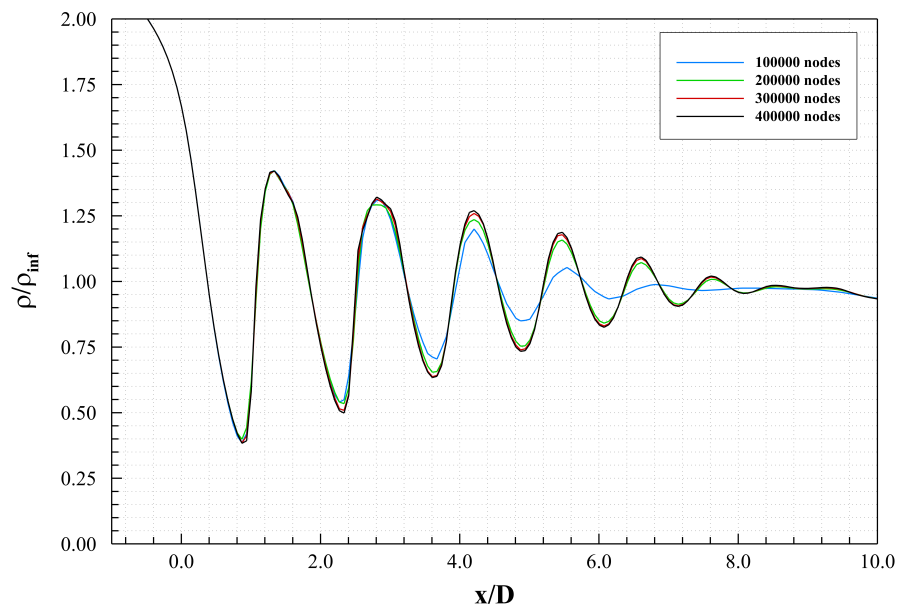


Figure 1.15: Comparison between computational grids - Density

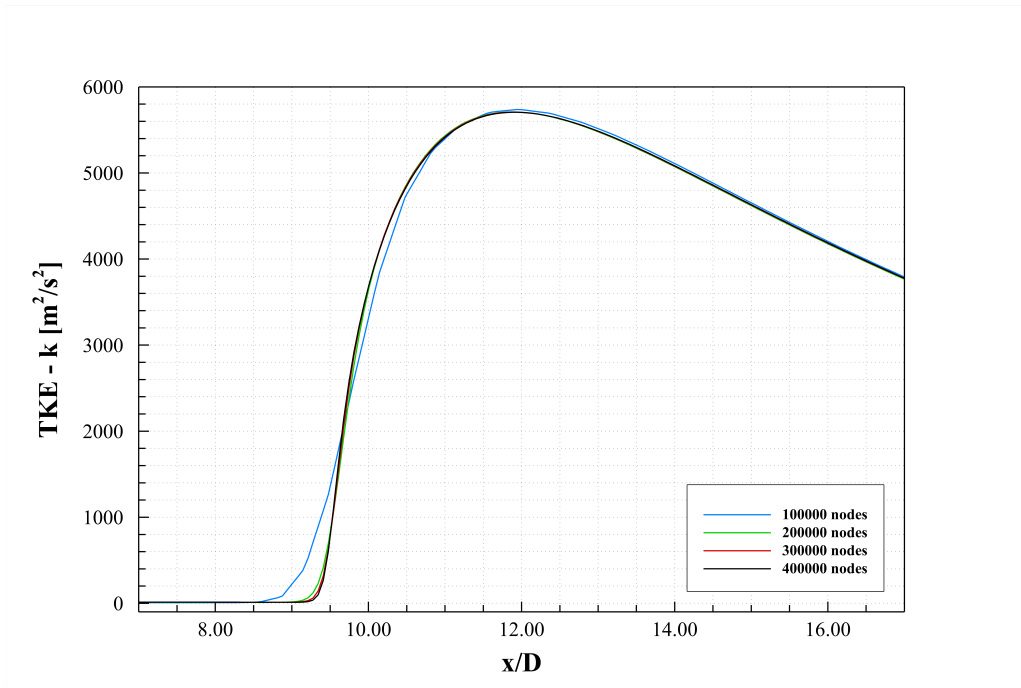


Figure 1.16: Comparison between computational grids - Turbulent Kinetic Energy

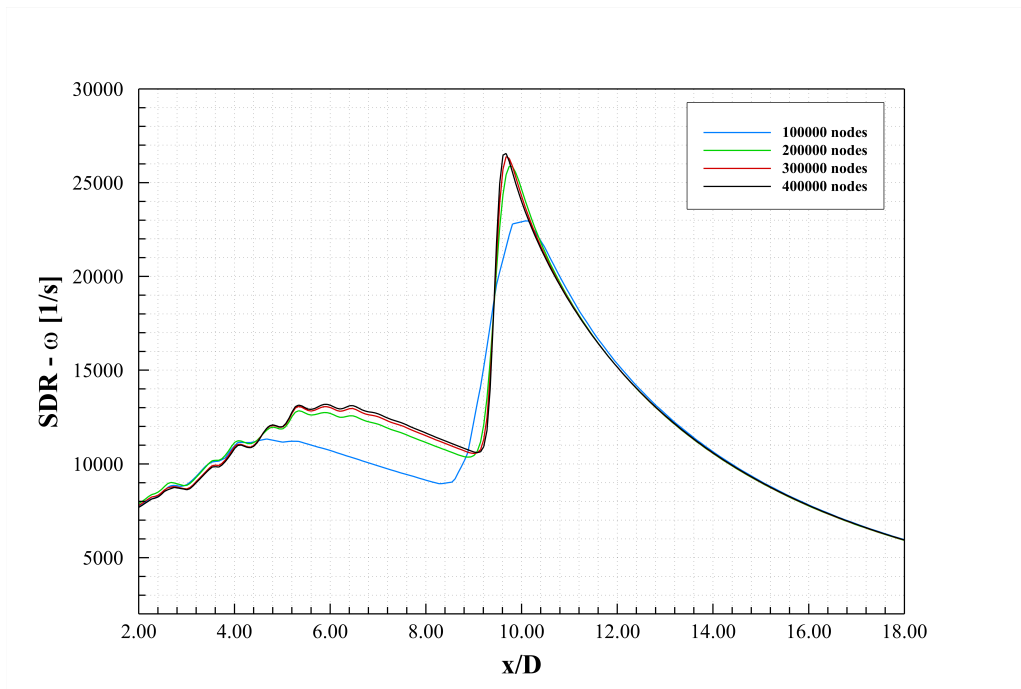


Figure 1.17: Comparison between computational grids - Specific Dissipation Rate

1.4.6 Comparison with Reference Data

In this last paragraph, a comparison with the reference solution of the same fluid dynamics test case performed by Fluent and SU2 is made. In Fluent two simulations are done, with and without compressibility correction model by Sarkar²¹. In the open-source SU2 software there is still no compressibility correction model, hence a standard Menter SST⁹ turbulence model is used. All these simulations are compared with the reference one performed by Miller¹⁰. Contour lines are displayed but some comparisons are done also along some particular lines.

In the following contour diagrams from Figure 1.18 to Figure 1.22:

- black lines: reference solution by Miller¹⁰
- red lines: Fluent solution with Compressibility Correction
- green lines: Fluent solution without Compressibility Correction
- blue lines: SU2 solution

The reference solution is performed with the software FUN3D and with the compressibility correction model developed by Wilcox²⁴.

From the following images it can be seen that all three solutions performed match the reference data with some discrepancies because of different computational grid, numerical effects and different model for compressibility correction used by Fluent. Greater disparities can be seen in the ω contour where the reference solution gives an under-predicted results due to the use of wall-function model.

In the figures below the mean physical quantities variation is represented along the axis line and along a radial direction in order to evaluate the variation in the shear layer.

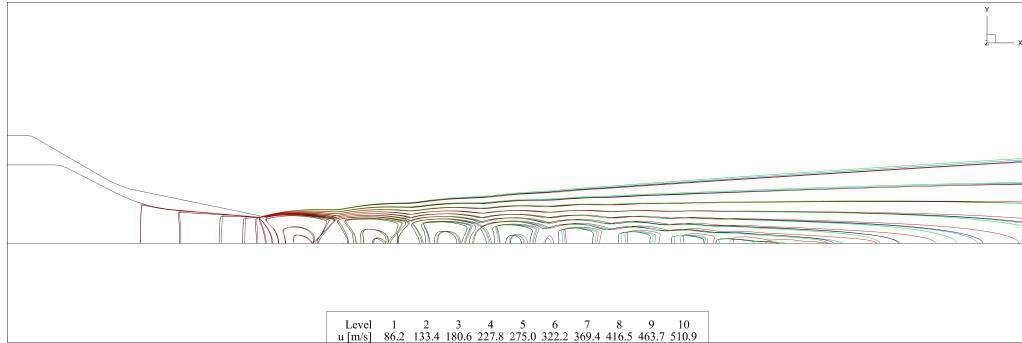


Figure 1.18: Comparison with reference data of Miller¹⁰ - Axial Velocity

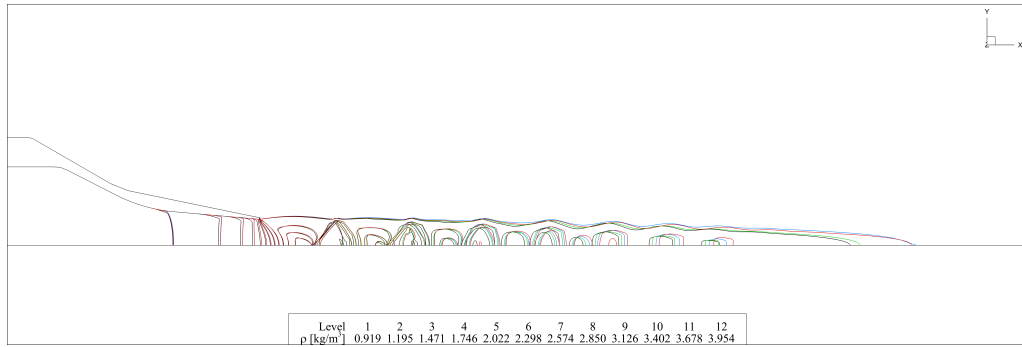


Figure 1.19: Comparison with reference data of Miller¹⁰ - Density

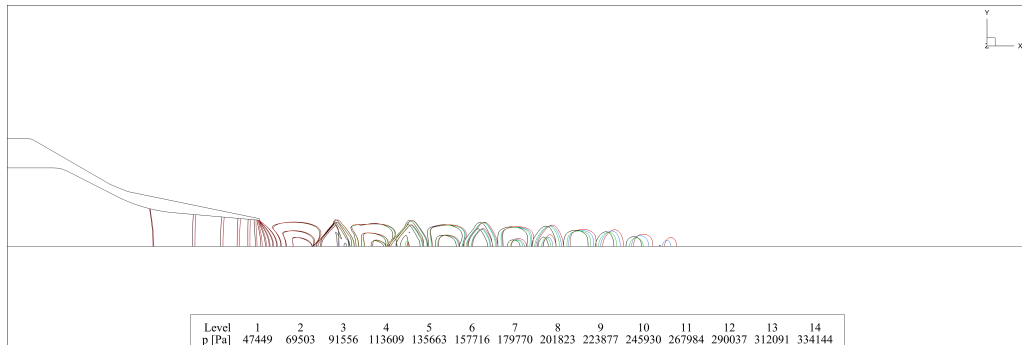


Figure 1.20: Comparison with reference data of Miller¹⁰ - Static Pressure

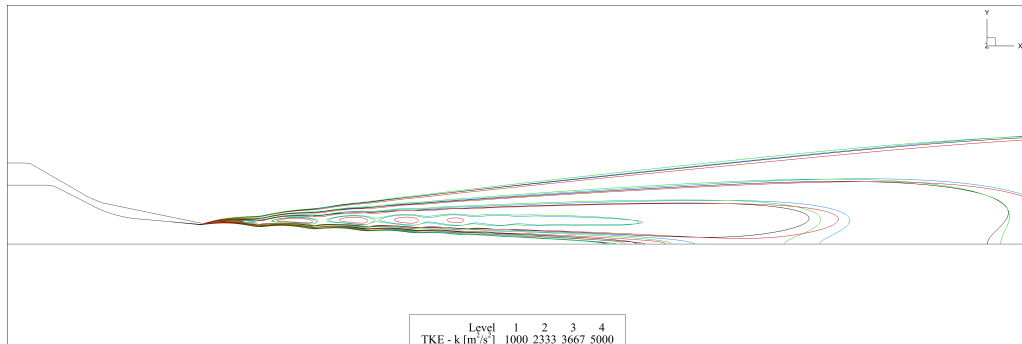


Figure 1.21: Comparison with reference data of Miller¹⁰ - Turbulent Kinetic Energy

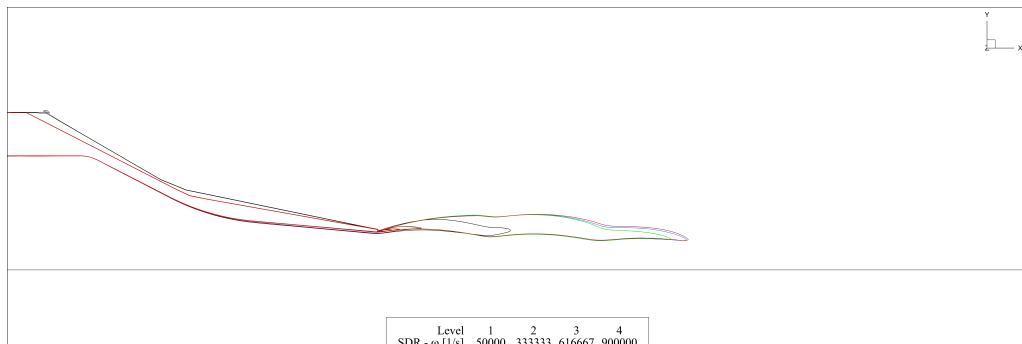


Figure 1.22: Comparison with reference data of Miller¹⁰ - Specific Dissipation Rate

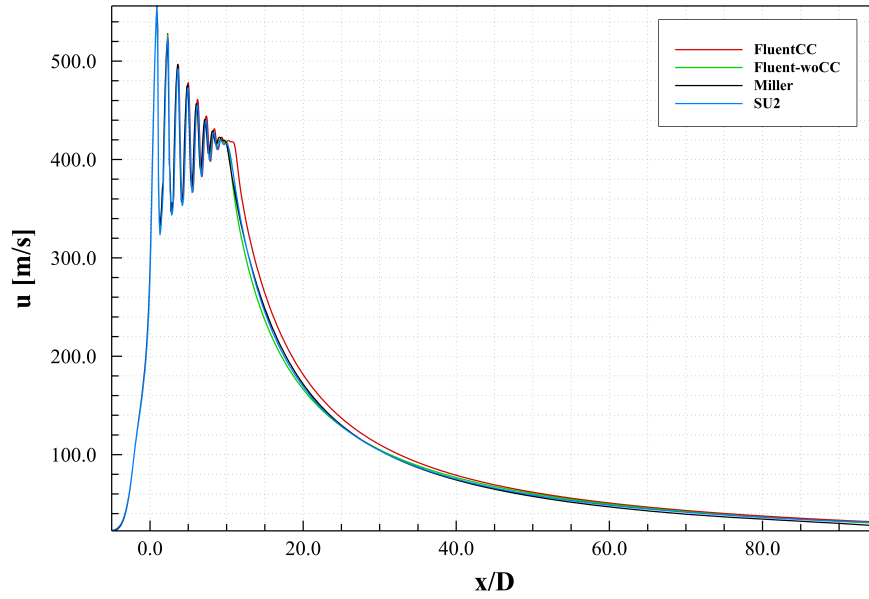


Figure 1.23: Comparison with reference data of Miller¹⁰ - Plot along $y = 0$ - Axial Velocity

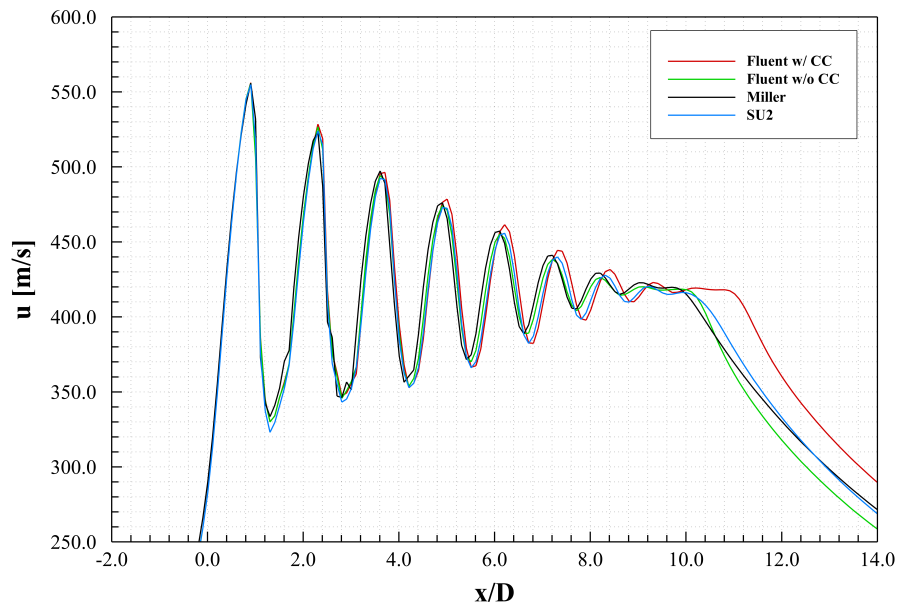


Figure 1.24: Comparison with reference data of Miller¹⁰ - Plot along $y = 0$ - Axial Velocity - Deep View

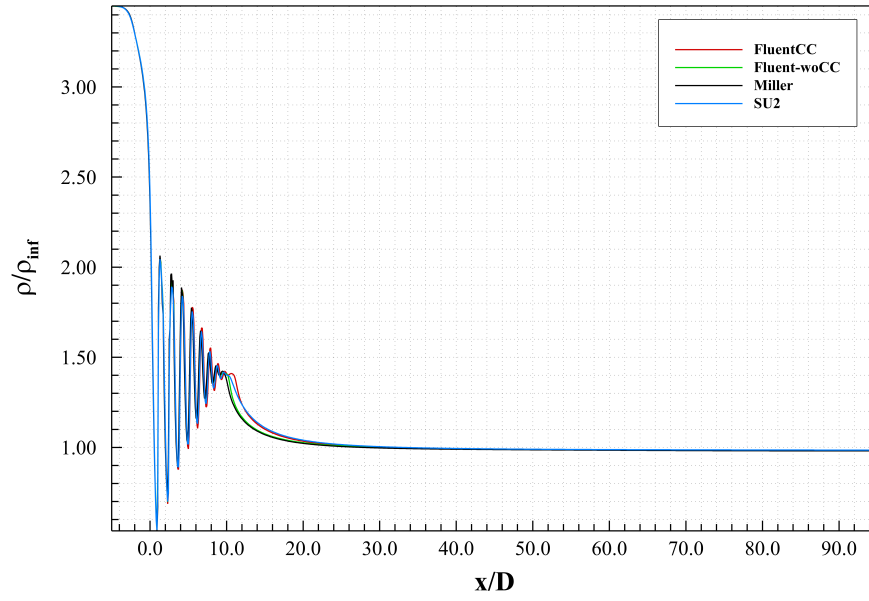


Figure 1.25: Comparison with reference data of Miller¹⁰ - Plot along $y = 0$ - Density

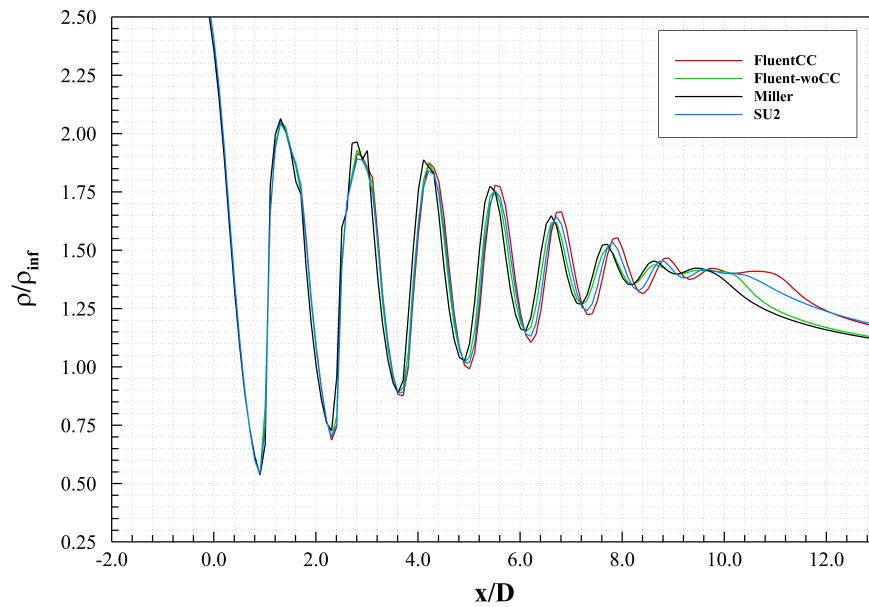


Figure 1.26: Comparison with reference data of Miller¹⁰ - Plot along $y = 0$ - Density - Deep View

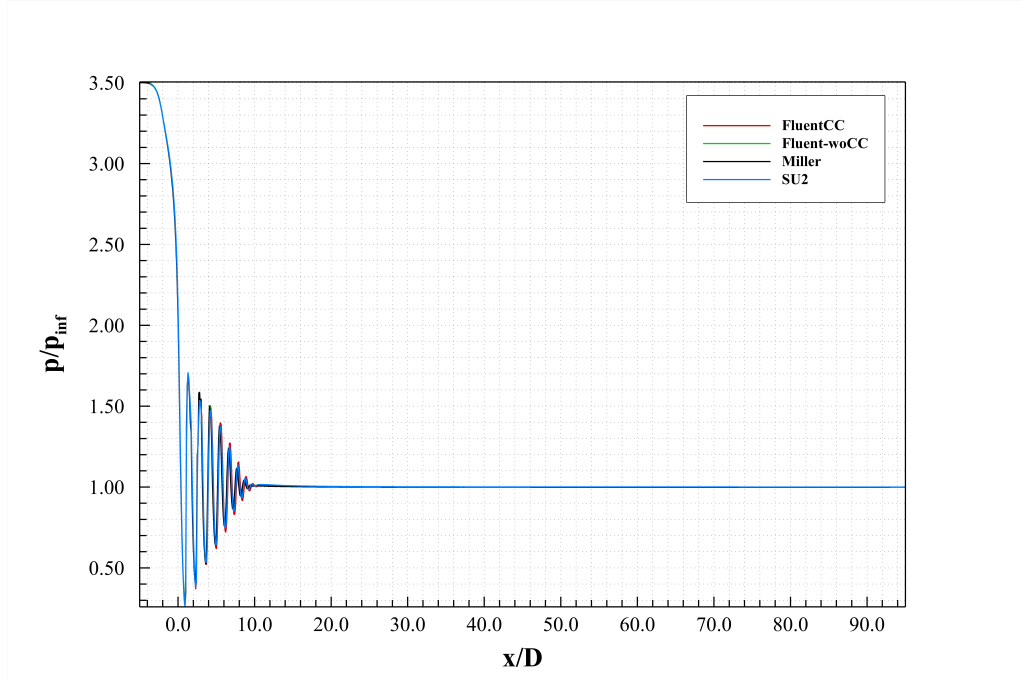


Figure 1.27: Comparison with reference data of Miller¹⁰ - Plot along $y = 0$ - Static Pressure

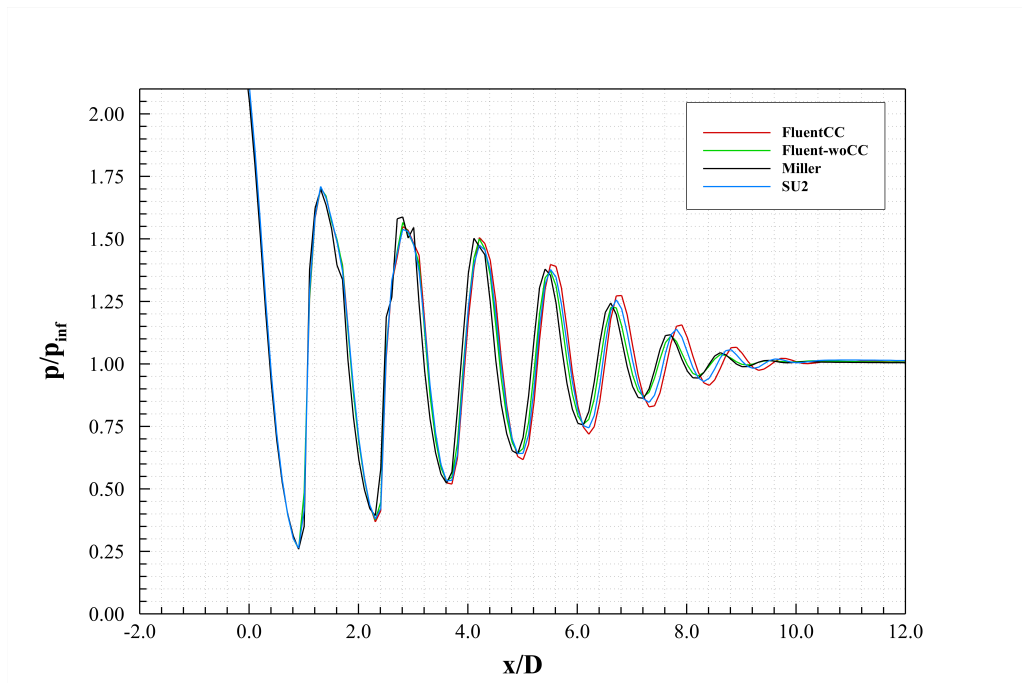


Figure 1.28: Comparison with reference data of Miller¹⁰ - Plot along $y = 0$ - Static Pressure - Deep View

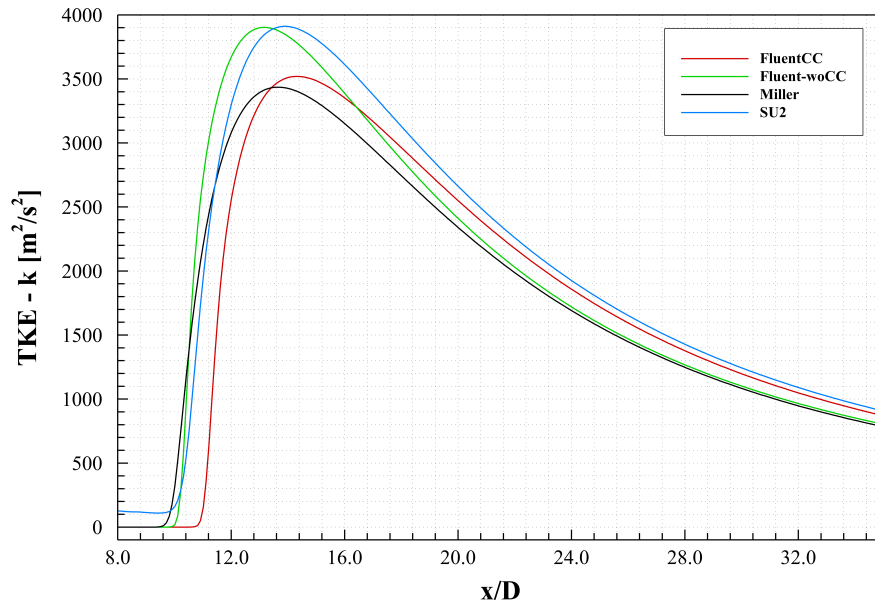


Figure 1.29: Comparison with reference data of Miller¹⁰ - Plot along $y = 0$ - Turbulent Kinetic Energy

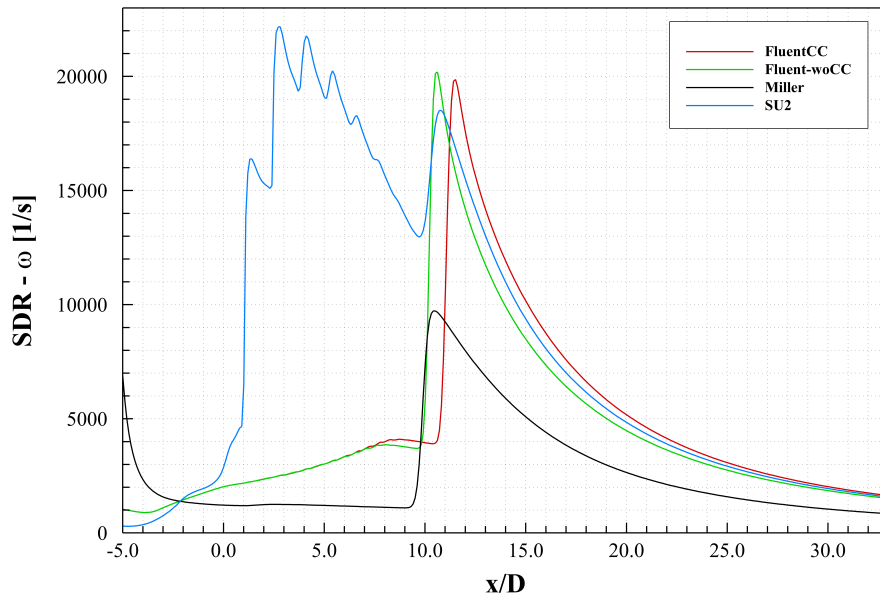


Figure 1.30: Comparison with reference data of Miller¹⁰ - Plot along $y = 0$ - Specific Dissipation Rate

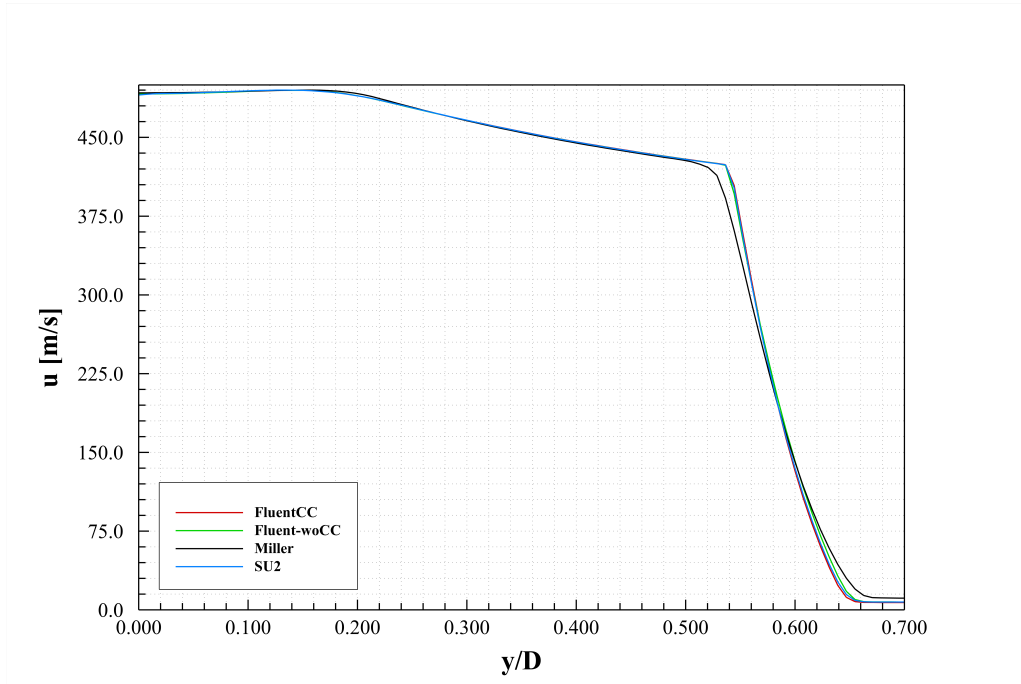


Figure 1.31: Comparison with reference data of Miller¹⁰ - Plot along $x = 0.03$ - Axial Velocity

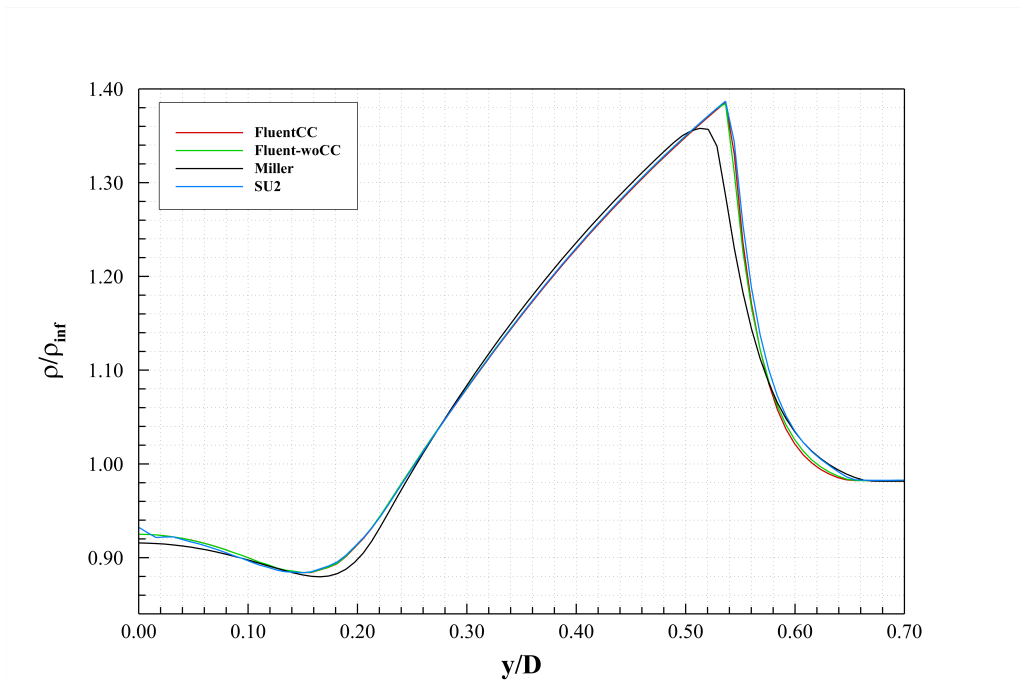


Figure 1.32: Comparison with reference data of Miller¹⁰ - Plot along $x = 0.03$ - Density

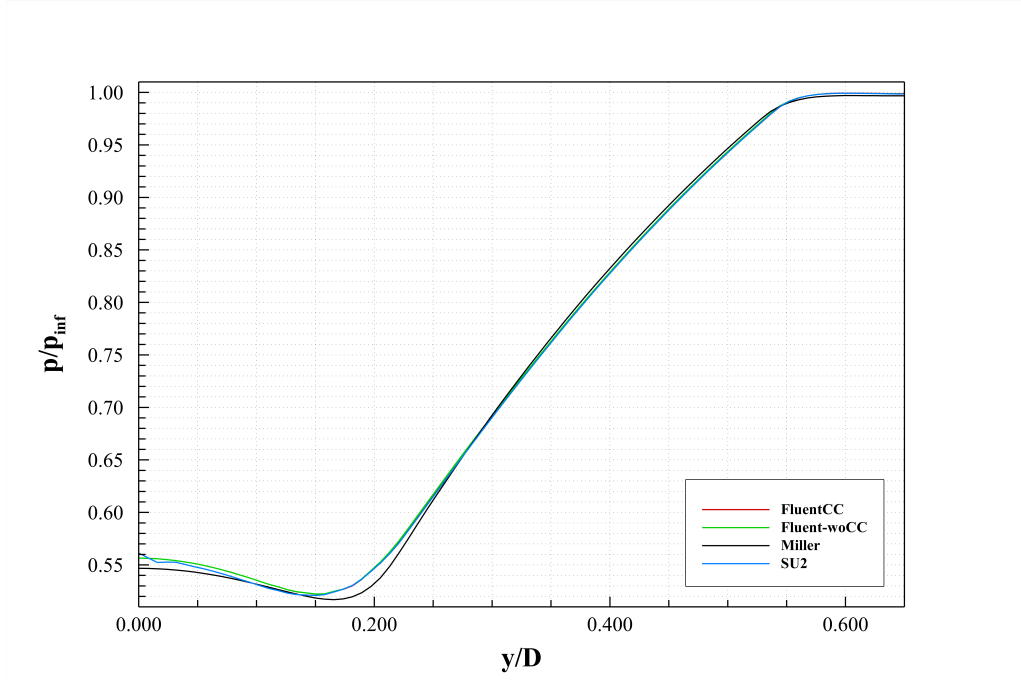


Figure 1.33: Comparison with reference data of Miller¹⁰ - Plot along $x = 0.03$ - Static Pressure

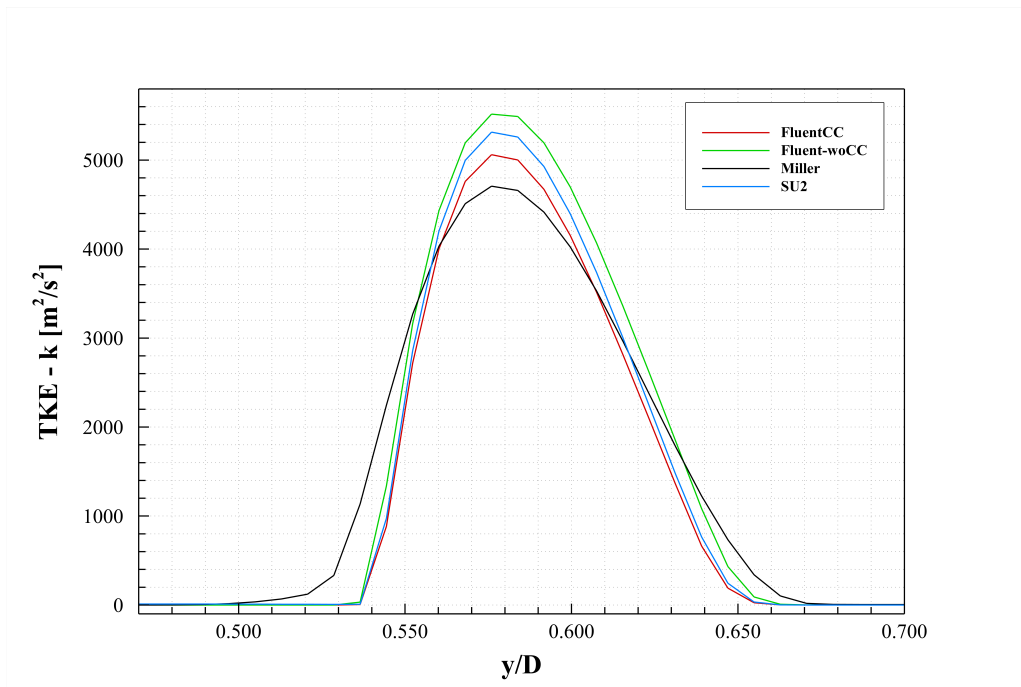


Figure 1.34: Comparison with reference data of Miller¹⁰ - Plot along $x = 0.03$ - Turbulent Kinetic Energy

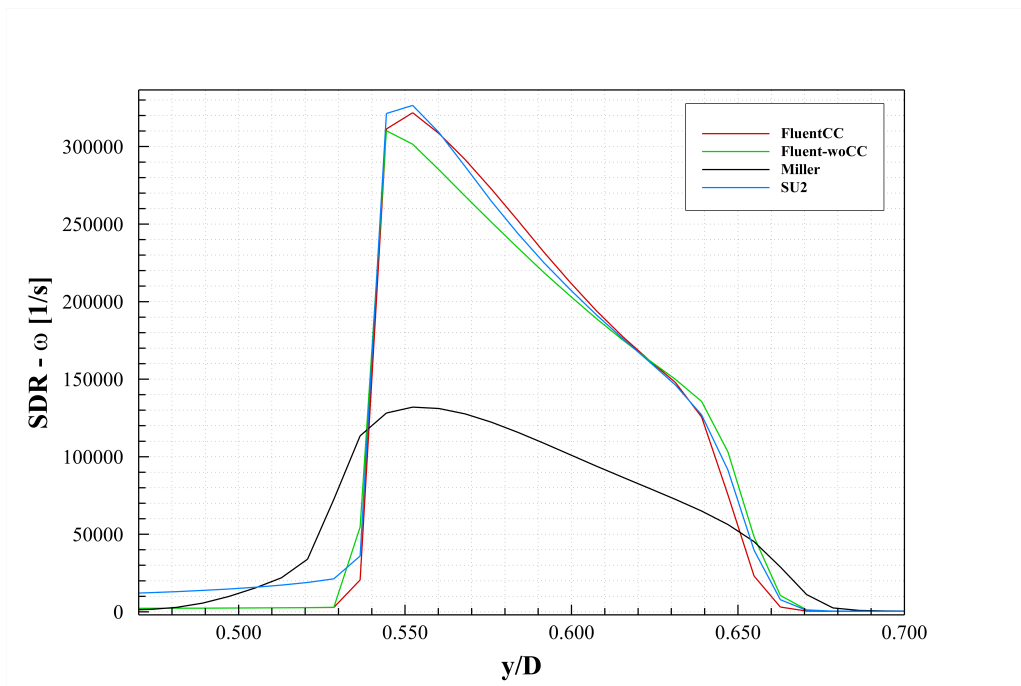


Figure 1.35: Comparison with reference data of Miller¹⁰ - Plot along $x = 0.03$ - Specific Dissipation Rate

Chapter 2

Aeroacoustics Analogy for Jet-Noise Prediction

The prediction of jet-noise has been the object of continuous interest and study since the introduction of the jet engine for commercial use.

For under-expanded jets the noise can be addressed to:

- Mixing noise: induced by the turbulent mixing in the jet itself. It is dominant in the downstream direction.
- Broad-Band Shock-Associated noise (BBSAN): induced by the interaction between shock-cell structures and shear layer. It is dominant at the sideline and upstream direction at mid to high frequencies.
- Discrete Component (Screech): caused by a feedback loop consisting of acoustic waves propagating upstream due to their reflection by shock waves and consequently being reflected downstream by the air-frame or nozzle. It is observed in the spectra when the jet is operating off-design.

Acoustic analogies are a practicable methods to predict noise generated by a jet flow and are formulated rearranging the equations of motion for a compressible fluid, usually splitting sources from propagation effects. By definition, this rearrangement results in a set of equivalent sources that are assumed to be non negligible in a limited region of space.

According to this, sound propagation needs to be addressed independently from its generation. In practice, noise sources are first identified, with the help of a RANS solution, and the propagation of sound over a quiescent base flow is addressed subsequently.

In that way, acoustic analogies are able to describe a one-way energy conversion from the fluid kinetic energy to sound, and the back-reaction of acoustics on the base flow is not accounted for. Hence, in this work, ‘Discrete Components’ are not taken into account. Therefore, configuration for which acoustic feedback mechanisms are crucial, like screeching supersonic jets or noise from cavities, cannot be tackled with such an approach.

The acoustic analogy developed is based on the Euler equations and contains two independent source models which predict the noise from turbulence (mixing noise) and shock-wave shear layer interactions (BBSAN). Propagation effects should be considered by calculating the vector Green’s function of the linearized Euler equations.

In addition, a statistical model of the two-point cross-correlation of the velocity fluctuations is used to describe the turbulence.

As previously mentioned, the acoustic analogy is partially informed by three-dimensional steady Reynolds-Averaged Navier-Stokes solution that include the nozzle geometry.

2.1 Mathematical Theory

The following acoustic analogy is based on the work of Morris and Farassat¹³. The governing equations, in the hypothesis of adiabatic and inviscid flow, are the Euler equations:

$$\frac{\partial \pi}{\partial t} + u_j \frac{\partial \pi}{\partial x_j} + \frac{\partial u_i}{\partial x_i} = 0 \quad (2.1)$$

$$\frac{\partial u_i}{\partial t} + u_j \frac{\partial u_i}{\partial x_j} + a^2 \frac{\partial \pi}{\partial x_i} = 0 \quad (2.2)$$

where $\pi = \gamma^{-1} \ln(p/p_\infty)$ and a is the speed of the sound.

Using Reynolds' decomposition it is possible to linearize the governing equations about a mean flow.

$$\pi = \bar{\pi} + \pi'; \quad u_i = \bar{u}_i + u'_i; \quad a = \bar{a} + a' \quad (2.3)$$

where overbars denote mean quantities and the primes indicate the fluctuations about the mean. Substituting equations (2.3) in equations (2.1)-(2.2) and retaining on the left hand side of equations only terms which are linear in fluctuation, the inhomogeneous linearized Euler equations are obtained:

$$\frac{\partial \pi'}{\partial t} + \bar{u}_j \frac{\partial \pi'}{\partial x_j} + \frac{\partial u'_i}{\partial x_i} = \theta \quad (2.4)$$

$$\frac{\partial u'_i}{\partial t} + \bar{u}_j \frac{\partial u'_i}{\partial x_j} + u'_j \frac{\partial \bar{u}_i}{\partial x_j} + \bar{a}^2 \frac{\partial \pi'}{\partial x_i} = f_i \quad (2.5)$$

On the right hand side of equations (2.4)-(2.5) there are the dilatation rate term (θ) and the unsteady force per unit of mass (f_i) respectively. In both of them only the second order fluctuations are considered to contribute to the sound field.

2.1.1 Sources Terms: Mixing Noise

For mixing noise, terms on the right hand side of equations (2.4)-(2.5) can be written as follows:

$$\theta = -u'_i \frac{\partial \pi'}{\partial x_i} \quad (2.6)$$

$$f_i = \frac{\partial}{\partial x_i} \left(\frac{u'_j u'_j}{2} \right) - \varepsilon_{ijk} u_j \omega_k + a'^2 \frac{\partial \pi'}{\partial x_i} \quad (2.7)$$

The equivalent source associated with scattering of pressure fluctuations by fluctuations in the speed of sound is neglected. In that approach, the dilatation rate source and the three components of the unsteady forces in the linearized momentum equations are all uncorrelated. Therefore, the auto-correlation of the far-field pressure can be written as the sum of the individual auto-correlations.

2.1.2 Sources Terms: Broad-Band Shock Associated Noise

Broadband shock-associated noise (BBSAN) is a component of jet noise for supersonic jets operating at off-design conditions. The degree of off-design conditions is quantified by the factor β , where

$$\beta = \sqrt{|M_j^2 - M_d^2|} \quad (2.8)$$

The interaction between the large turbulence structures and the quasi-periodic shock cells gives rise to time-dependent disturbances, hence, the flow quantities consist of four main components:

$$\pi = \bar{\pi} + \pi_s + \pi_t + \pi' \quad (2.9)$$

$$u_i = \bar{u}_i + u_{si} + u_{ti} + u'_i \quad (2.10)$$

$$a = \bar{a} + a_s + a_t + a' \quad (2.11)$$

where the over-line denotes the long time averaged value, the subscript 's' denotes the perturbations associated with the shock cell structure, the subscript 't' denotes the fluctuations associated with the turbulence, and the primes denote the fluctuations generated by the interaction of the turbulence and the shock cell structure.

It will be assumed that the shock cell structure satisfies the steady linearized

version of equation (2.1)-(2.2). In addition, it is assumed that the unsteady linearized version of these equations is also satisfied by the turbulent velocity fluctuations (v_t). This is justified if the important components of turbulence, in terms of broadband shock-associated noise, are consistent over relatively large axial distances. These components are described well by a linear instability wave model.

Making these assumptions, the inhomogeneous equations for the fluctuations associated with the interaction of the turbulence with the shock cells can be solved.

For broad-band shock associated noise, terms on the right hand side of equation (2.4) can be written as follows:

$$\theta = -u_{sj} \frac{\partial \pi_t}{\partial x_j} - u_{tj} \frac{\partial \pi_s}{\partial x_j} \quad (2.12)$$

where θ is a dilatation rate generated by the interaction between the pressure gradients and the turbulent velocity perturbations and the shock cells.

The unsteady force per unit of mass in the equation (2.5) can be divided in two main terms:

$$f_i = f_i^v + f_i^a \quad (2.13)$$

f_i^v is the unsteady force per unit volume associated with interactions between the turbulent velocity fluctuations and the velocity perturbations associated with the shock cells.

f_i^a is the unsteady force per unit volume related to the interaction of fluctuations in the sound speed (or temperature), caused by the turbulence and the shock cells, and the associated pressure gradients.

$$f_i^v = -u_{sj} \frac{\partial u_{ti}}{\partial x_j} - u_{tj} \frac{\partial u_{si}}{\partial x_j} \quad (2.14)$$

$$f_i^a = -a_s^2 \frac{\partial \pi_t}{\partial x_i} - a_t^2 \frac{\partial \pi_s}{\partial x_i} \quad (2.15)$$

In traditional approaches to turbulence mixing noise models these equivalent sources have been treated separately and the same assumption is made here.

2.1.3 Solution of Aeroacoustics Equations

Once the acoustic analogy model has been chosen and the source terms have been defined, the equations' system must be solved to evaluate the acoustic propagation. The expressions (2.4)-(2.5) are not homogeneous and a method to solve them is to introduce the Green's functions.

The vector Green's function of the LEE is defined as

$$\frac{\partial \pi_g^n}{\partial t} + \bar{u}_j \frac{\partial \pi_g^n}{\partial x_j} + \frac{\partial u_{gi}^n}{\partial x_i} = \delta(\mathbf{x} - \mathbf{y}) \delta(t - \tau) \delta_{0n} \quad (2.16)$$

$$\frac{\partial u_{gi}^n}{\partial t} + \bar{u}_j \frac{\partial u_{gi}^n}{\partial x_j} + u_{gj}^n \frac{\partial \bar{u}_i}{\partial x_j} + \bar{a}^2 \frac{\partial \pi_g^n}{\partial x_i} = \delta(\mathbf{x} - \mathbf{y}) \delta(t - \tau) \delta_{in} \quad (2.17)$$

where $\pi_g^n = \pi_g^n(\mathbf{x}, \mathbf{y}, t - \tau)$ and $u_{gi}^n = u_{gi}^n(\mathbf{x}, \mathbf{y}, t - \tau)$ are the components of the vector Green's function; \mathbf{x} denotes the observer position; \mathbf{y} denotes the source location; $\delta()$ is the Dirac delta function; τ is the source emission time and δ_{ij} is the Kronecker delta function.

Let the vector Green's function be periodic, the Fourier transform (FT) and the inverse Fourier transform (IFT) can be respectively expressed as follows:

$$\pi_g^n(\mathbf{x}, \mathbf{y}, \omega) = \int_{-\infty}^{\infty} \pi_g^n(\mathbf{x}, \mathbf{y}, t, \tau) \exp[-i\omega(t - \tau)] d\tau \quad (2.18)$$

$$\pi_g^n(\mathbf{x}, \mathbf{y}, t, \tau) = \frac{1}{2\pi} \int_{-\infty}^{\infty} \pi_g^n(\mathbf{x}, \mathbf{y}, \omega) \exp[i\omega(t - \tau)] d\omega \quad (2.19)$$

Once each component of the vector Green's function is known, it is simple to write the fluctuating far-field pressure as a convolution integral of Green's functions and the equivalent sources.

$$p'(\mathbf{x}, t) = \gamma p_{\infty} \int_{-\infty}^{\infty} \cdots \int_{-\infty}^{\infty} \pi_g^0(\mathbf{x}, \mathbf{y}, t, \tau) \theta(\mathbf{y}, \tau) + \sum_{n=1}^3 \pi_g^n(\mathbf{x}, \mathbf{y}, t, \tau) f_n(\mathbf{y}, \tau) d\tau d\mathbf{y} \quad (2.20)$$

The spectral density is defined as the Fourier transform of the auto-correlation of the fluctuating pressure. It is a function of the observer location (\mathbf{x}) and the angular frequency (ω).

$$S(\mathbf{x}, \omega) = \int_{-\infty}^{\infty} \overline{p'(\mathbf{x}, t) p'(\mathbf{x}, t + \tau)} \exp[-i\omega\tau] d\tau \quad (2.21)$$

Combining the equation (2.20) and the equation (2.21)

$$\begin{aligned}
S(\mathbf{x}, \omega) = & \rho_\infty^2 a_\infty^4 \int_{-\infty}^{\infty} \cdots \int_{-\infty}^{\infty} \left\{ \pi_g^0(\mathbf{x}, \mathbf{y}, -\omega) \pi_g^0(\mathbf{x}, \mathbf{y} + \boldsymbol{\eta}, \omega) \overline{\theta(\mathbf{y}, \tau) \theta(\mathbf{y} + \boldsymbol{\eta}, t + \tau)} \right. \\
& + \sum_{n=1}^3 \sum_{m=1}^3 \pi_g^n(\mathbf{x}, \mathbf{y}, -\omega) \pi_g^m(\mathbf{x}, \mathbf{y} + \boldsymbol{\eta}, \omega) \overline{f_n(\mathbf{y}, \tau) f_m(\mathbf{y} + \boldsymbol{\eta}, t + \tau)} \left. \right\} \\
& \times \exp[-i\omega\tau] d\tau d\boldsymbol{\eta} d\mathbf{y} \quad (2.22)
\end{aligned}$$

where $\boldsymbol{\eta} = (\xi, \eta, \zeta)$ is introduced to evaluate the auto-correlation and represents the distance between two different close source points \mathbf{y}_1 and \mathbf{y}_2 in the source region.

By definition, for the periodic vector Green's function of the LEE is:

$$\pi_g^{n*}(\mathbf{x}, \mathbf{y}, \omega) = \pi_g^n(\mathbf{x}, \mathbf{y}, -\omega) \quad (2.23)$$

where the '*' indicates the complex conjugate of each component.

Following the work of Tam and Auriault²³ and assuming that the observer (\mathbf{x}) is in the far-field relative to the source (\mathbf{y}), the two closely placed source points in the jet can be related due to a phase difference assessed by ray acoustics. Figure 2.1 shows the rays from a faraway point \mathbf{x} to \mathbf{y}_1 and \mathbf{y}_2 . The rays are essentially parallel except after entering the jet flow. The paths for the rays to \mathbf{y}_1 and \mathbf{y}_2 differ by a length nearly equal to

$$AC = \frac{\mathbf{x} \cdot \boldsymbol{\eta}}{|\mathbf{x}|} = \frac{x_1\xi + x_2\eta + x_3\zeta}{x} \quad (2.24)$$

According to this the next expression can be derived.

$$\pi_g^m(\mathbf{x}, \mathbf{y} + \boldsymbol{\eta}, \omega) \simeq \pi_g^m(\mathbf{x}, \mathbf{y}, \omega) \exp \left[\frac{-i\omega}{a_\infty x} (x_1\xi + x_2\eta + x_3\zeta) \right] \quad (2.25)$$

Using equation (2.23) and equation (2.25) in the expression of the spectral

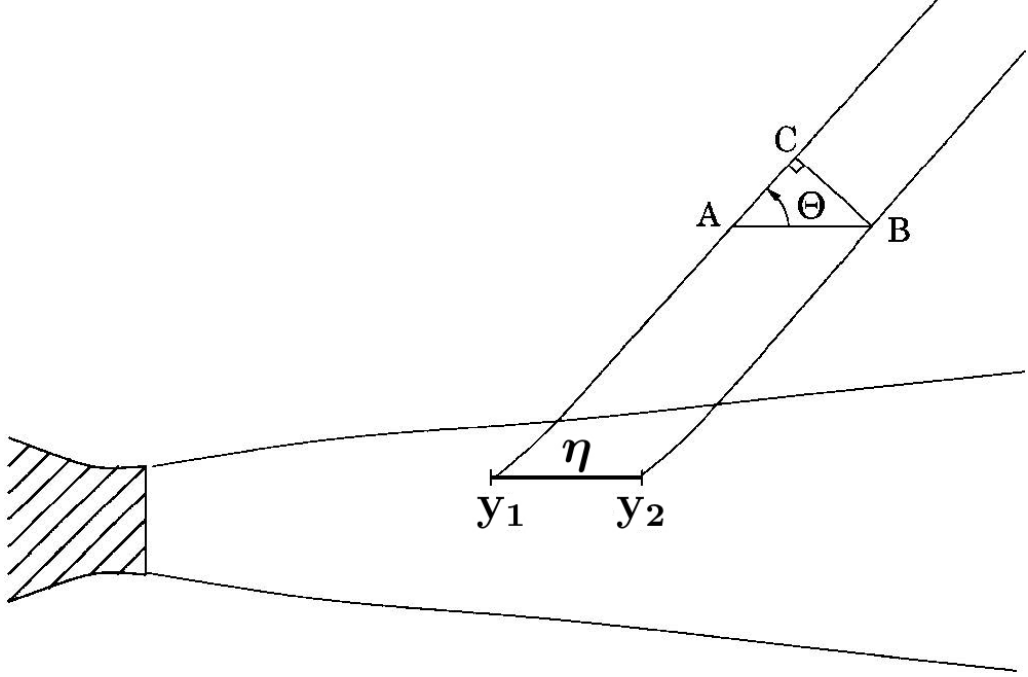


Figure 2.1: Phase delay due to the η distance between the two source points

density:

$$\begin{aligned}
 S(\mathbf{x}, \omega) = & \rho_{\infty}^2 a_{\infty}^4 \int_{-\infty}^{\infty} \cdots \int_{-\infty}^{\infty} \left\{ \pi_g^{*0}(\mathbf{x}, \mathbf{y}, \omega) \pi_g^0(\mathbf{x}, \mathbf{y}, \omega) \overline{\theta(\mathbf{y}, \tau) \theta(\mathbf{y} + \boldsymbol{\eta}, t + \tau)} \right. \\
 & + \left. \sum_{n=1}^3 \sum_{m=1}^3 \pi_g^{*n}(\mathbf{x}, \mathbf{y}, \omega) \pi_g^m(\mathbf{x}, \mathbf{y}, \omega) \overline{f_n(\mathbf{y}, \tau) f_m(\mathbf{y} + \boldsymbol{\eta}, t + \tau)} \right\} \\
 & \times \exp \left[\frac{-i\omega}{a_{\infty} x} (x_1 \xi + x_2 \eta + x_3 \zeta) \right] \exp [-i\omega \tau] d\tau d\boldsymbol{\eta} d\mathbf{y} \quad (2.26)
 \end{aligned}$$

2.1.4 Mixing Noise: Modeling of Auto-correlation Terms

Morris and Boluriaan¹² have developed a model for the dilatation rate (2.27) and the unsteady force per unit mass (2.28) in order to evaluate the mixing noise contribution.

$$\overline{\theta(\mathbf{y}, \tau)\theta(\mathbf{y} + \boldsymbol{\eta}, t + \tau)} = A_s^2 \frac{(u_s/a_\infty)^4}{\tau_s^2} E(\boldsymbol{\eta}, \tau) \quad (2.27)$$

$$\overline{f_n(\mathbf{y}, \tau)f_m(\mathbf{y} + \boldsymbol{\eta}, t + \tau)} = B_s^2 \frac{(u_s/a_\infty)^2 u_s^2}{l_x^2} E(\boldsymbol{\eta}, \tau) \quad (2.28)$$

where $E(\boldsymbol{\eta}, \tau)$ can be also modeled according to Ribner's²⁰ postulate, separating the spatial and temporal terms:

$$E(\boldsymbol{\eta}, \tau) = \exp\left[-\frac{|\tau|}{\tau_s}\right] \exp\left[-\frac{(\xi - \bar{u}\tau)^2}{l_x^2}\right] \exp\left[-\frac{(\eta - \bar{v}\tau)^2}{l_y^2}\right] \exp\left[-\frac{(\zeta - \bar{w}\tau)^2}{l_z^2}\right] \quad (2.29)$$

The integration involving $\boldsymbol{\eta}$ and τ in the equation (2.30) can be performed analytically

$$\begin{aligned} & \int_{-\infty}^{\infty} \cdots \int_{-\infty}^{\infty} \exp\left[-\frac{|\tau|}{\tau_s}\right] \exp\left[-\frac{(\xi - \bar{u}\tau)^2}{l_x^2}\right] \exp\left[-\frac{(\eta - \bar{v}\tau)^2}{l_y^2}\right] \\ & \times \exp\left[-\frac{(\zeta - \bar{w}\tau)^2}{l_z^2}\right] \exp\left[\frac{-i\omega}{a_\infty x} (x_1\xi + x_2\eta + x_3\zeta)\right] \exp[-i\omega\tau] d\boldsymbol{\eta} d\tau \end{aligned} \quad (2.30)$$

and results in

$$\begin{aligned} & \frac{2\pi^{3/2} a_\infty^2 l_x l_y l_z x^2 \tau_s}{a_\infty^2 x^2 + (a_\infty x + \bar{u}x_1 + \bar{v}x_2 + \bar{w}x_3)^2 \tau_s^2 \omega^2} \\ & \times \exp\left[-\frac{\omega^2 (l_x^2 x_1^2 + l_y^2 x_2^2 + l_z^2 x_3^2)}{4a_\infty^2 x^2}\right] \end{aligned} \quad (2.31)$$

These assumptions are needed for the integration

$$\tau_s > 0; l_i > 0; a_\infty > 0; x > 0$$

These are rational assumptions from a physical point of view, since the turbulent kinetic energy in the limit is zero and the model simply considers the jet flow at $x > 0$, where $x = 0$ represents the nozzle outlet.

Thus, the spectral density for the mixing noise component can be written as

$$\begin{aligned}
S(\mathbf{x}, \omega) = & \rho_\infty^2 a_\infty^4 \int_{-\infty}^{\infty} \int_{-\infty}^{\infty} \int_{-\infty}^{\infty} \frac{2\pi^{3/2} a_\infty^2 l_x l_y l_z x^2 \tau_s}{a_\infty^2 x^2 + (a_\infty x + \bar{u}x_1 + \bar{v}x_2 + \bar{w}x_3)^2 \tau_s^2 \omega^2} \\
& \times \left\{ \pi_g^{*0}(\mathbf{x}, \mathbf{y}, \omega) \pi_g^0(\mathbf{x}, \mathbf{y}, \omega) A_s^2 \frac{(u_s/a_\infty)^4}{\tau_s^2} + \sum_{n=1}^3 \sum_{m=1}^3 \pi_g^{*n}(\mathbf{x}, \mathbf{y}, \omega) \pi_g^m(\mathbf{x}, \mathbf{y}, \omega) \right. \\
& \left. \times B_s^2 \frac{(u_s/a_\infty)^2 u_s^2}{l_x^2} \right\} \exp \left[-\frac{\omega^2 (l_x^2 x_1^2 + l_y^2 x_2^2 + l_z^2 x_3^2)}{4 a_\infty^2 x^2} \right] d\mathbf{y} \quad (2.32)
\end{aligned}$$

In the expression (2.32) colors have been used to understand better the origin of variables, in particular:

- Blue is used to highlight input variables
- Red is used to highlight variables that are either directly computable or derived from the CFD
- Green is used to highlight asymptotic variables
- Cyan is used to highlight empirical constants

Due to the use of a simplified vector Green's function that does not account for mean flow refraction effects, an empirical correction proposed by Kandula and Vu⁶ is used to scale correctly the mixing noise with the location of the observer. The following expression is implemented and scales the spectral densities.

$$C = [(1 - M_c \cos \theta)^2 + \alpha^2 M_c^2]^{0.5\beta} \quad (2.33)$$

In the equation(2.33) M_c is the convective Mach number and θ is the polar angle of observer (figure 2.2). Two constants have to be chosen, and it is seen that a good predictions can be obtained with these ones.

$$\alpha = 0.4; \quad \beta = -5 \quad (2.34)$$

2.1.5 BBSAN: Modeling of Auto-correlation Terms

Following the approach of Morris and Miller¹⁴, only the source terms associated with the velocity perturbations (2.14) are considered. It is expected that the scaling of the other source terms would be similar. The exception would be the source term associated with the temperature fluctuations (speed of sound fluctuations). The importance of this term remains the subject of debate in the prediction of turbulent mixing noise in heated jets. So, this term will not be considered further.

According to that, the perturbation pressure is given by

$$p'(\mathbf{x}, t) = \gamma p_\infty \int_{-\infty}^{\infty} \cdots \int_{-\infty}^{\infty} \sum_{n=1}^3 \pi_g^n(\mathbf{x}, \mathbf{y}, \omega) f_n^v(\mathbf{y}, \tau) d\omega d\tau d\mathbf{y} \quad (2.35)$$

By doing a dimensional analysis and taking into account the quantities on which the source terms depends on (perturbation velocity in the shear layer and perturbation pressure in the shock structure), the following expression can be derived:

$$f_i^v \simeq \frac{p_s v_t}{\rho_\infty a_\infty l_i} \quad (2.36)$$

where $p_s = p - p_\infty$ represents the shock cell strength, v_t is a characteristic turbulent velocity fluctuation, and l_i is a characteristic turbulent length scale. All of them can be retrieved from the RANS CFD solution.

Therefore, with the cross-correlation between the two source terms, a correlation between the perturbation velocities and a correlation between the perturbation pressures in the shock structure (p_s) is obtained.

Before proceeding it is necessary to examine the form of the two point cross correlation of f_v^n . It is dependent on the strength of the shock cells and the turbulent fluctuations, equation (2.36), and its product is significant in regions where the shocks and expansions intersect with the turbulent shear layer.

That is, if there is no turbulence present or pressure perturbation due to shock cells, then the term is small.

It is assumed that the two-point cross correlation function of the BBSAN source term can be written as:

$$\overline{f_n^v(\mathbf{y}, \tau) f_m^v(\mathbf{y} + \boldsymbol{\eta}, t + \tau)} = \frac{a_{nm} p_s(\mathbf{y}) p_s(\mathbf{y} + \boldsymbol{\eta}) K(\mathbf{y}) E(\boldsymbol{\eta}, \tau)}{\bar{\rho}^2 \bar{u}^2 l_x^2} \quad (2.37)$$

This is consistent with the statistics of the turbulence being locally a function

of the separation distance ($\boldsymbol{\eta}$) and time delay (τ) between the two source locations.

In order to emphasize the quasi-periodic nature of the shock cell structure and to assist in the implementation of the model, the axial spatial Fourier transform and its inverse function of the shock cell's pressure perturbation is defined.

$$\tilde{p}_s(k_1, y_2, y_3) = \int_{-\infty}^{\infty} p_s(\mathbf{y}) \exp[ik_1 y_1] dy_1 \quad (2.38)$$

$$p_s(\mathbf{y}) = \frac{1}{2\pi} \int_{-\infty}^{\infty} \tilde{p}_s(k_1, y_2, y_3) \exp[-ik_1 y_1] dy_1 \quad (2.39)$$

where k_1 is the wavenumber in the axial direction (y_1).

The more general expression of the spectral density due to the interaction between shear layer and shock cells, discarding the contribution of discrete tones, can be evaluated by substituting the equation (2.37) in the equation (2.22).

$$\begin{aligned} S(\mathbf{x}, \omega) = & \rho_{\infty}^2 a_{\infty}^4 \int_{-\infty}^{\infty} \int_{-\infty}^{\infty} \int_{-\infty}^{\infty} \frac{2\pi^{3/2} a_{\infty}^2 l_x l_y l_z x^2 \tau_s}{a_{\infty}^2 x^2 + (a_{\infty} x + \bar{u} x_1 + \bar{v} x_2 + \bar{w} x_3)^2 \tau_s^2 \omega^2} \\ & \times \left\{ \sum_{n=1}^3 \sum_{m=1}^3 \pi_g^{*n}(\mathbf{x}, \mathbf{y}, \omega) \pi_g^m(\mathbf{x}, \mathbf{y}, \omega) \frac{a_{mn} K(\mathbf{y}) p_s(\mathbf{y})}{2\pi \bar{\rho}^2 \bar{u}^2 l_x^2} \right. \\ & \times \left. \int_{-k_{1min}}^{k_{1max}} \tilde{p}_s(k_1, y_2, y_3) \exp[-ik_1 y_1] dk_1 \right\} \exp \left[-\frac{\omega^2 (l_x^2 x_1^2 + l_y^2 x_2^2 + l_z^2 x_3^2)}{4a_{\infty}^2 x^2} \right] d\mathbf{y} \end{aligned} \quad (2.40)$$

In this expression the term $p_s(\mathbf{y} + \boldsymbol{\eta})$ is substituted with $\tilde{p}_s(k_1, y_2, y_3)$ and the integration of $E(\boldsymbol{\eta}, \tau)$ is already performed.

The vector Green's functions (π_g^n) must be evaluated numerically for a given mean flow, often involving the locally parallel approximation or the full diverging flow.

BBSAN is radiated predominantly at large angles to the jet downstream axis, where the refractive effects of the mean flow would be small or absent. This can be performed by setting the mean flow conditions to their ambient values.

In view of this, the Green's function is approximated by the Green's function of the inhomogeneous Helmholtz equation (see appendix B), in the absence of a mean flow.

Another form of the spectral density is shown below and refers to the work

of Morris and Miller:¹⁴

$$\begin{aligned}
S(\mathbf{x}, \omega) = & \pi^{1/2} \rho_\infty^2 a_\infty^4 \int_{-\infty}^{\infty} \cdots \int_{-\infty}^{\infty} \left\{ \sum_{n=1}^3 \sum_{m=1}^3 \pi_g^{*n}(\mathbf{x}, \mathbf{y}, \omega) \pi_g^m(\mathbf{x}, \mathbf{y}, \omega) \frac{x^2}{x_n x_m} \times \right. \\
& \left. \frac{2K(\mathbf{y}) l_y l_z \tau_s}{3 \bar{\rho}^2 \bar{u}^2 l_x} p_s(\mathbf{y}) \tilde{p}_s(k_1, y_2, y_3) \right\} \frac{1}{\left[1 + \left(1 - \frac{\bar{u}}{a_\infty} \cos \theta + \frac{\bar{u} k_1}{\omega} \right)^2 \omega^2 \tau_s^2 \right]} \times \\
& \times \exp \left[-\frac{l_x^2}{4} \left(\frac{\omega}{a_\infty} \cos \theta - k_1 \right)^2 - \frac{\omega^2 l_y l_z}{4 a_\infty^2} \sin^2 \theta \right] dk_1 d\mathbf{y} \quad (2.41)
\end{aligned}$$

The final expression of the spectral density, substituting the expression (B.5) in the equation (2.41), is displayed in the following relation (2.42) and it considers

- Observer location in the far-field
- Absence of a mean flow (no refraction effects)
- Proudman¹⁸ form for isotropic turbulence: $a_{mn} \frac{x_n x_m}{x^2} = \frac{2}{3}$

$$\begin{aligned}
S(\mathbf{x}, \omega) = & \frac{1}{24\pi \sqrt{\pi} a_\infty^4 x^2} \int_{-\infty}^{\infty} \int_{-\infty}^{\infty} \int_{-\infty}^{\infty} \int_{-k_{1min}}^{k_{1max}} \frac{K l_y l_z}{l_x \tau_s} p_s(\mathbf{y}) \tilde{p}_s(k_1, y_2, y_3) \\
& \times \frac{\omega^2 \tau_s^2 \exp \left[\left(-\frac{l_x^2}{4} \left(\frac{\omega}{a_\infty} \cos \theta - k_1 \right)^2 - \frac{\omega^2 l_y l_z}{4 a_\infty^2} \sin^2 \theta \right) \right]}{1 + \left(1 - \frac{\bar{u}}{a_\infty} \cos \theta + \frac{\bar{u} k_1}{\omega} \right)^2 \omega^2 \tau_s^2} dk_1 d\mathbf{y} \quad (2.42)
\end{aligned}$$

In the equation (2.42) the observer location \mathbf{x} is written in spherical polar coordinates, given by

$$\mathbf{x} = x (\cos \theta, \sin \theta \cos \varphi, \sin \theta \sin \varphi) \quad (2.43)$$

where θ is the polar angle of observer (figure 2.2) and φ is the azimuth angle.

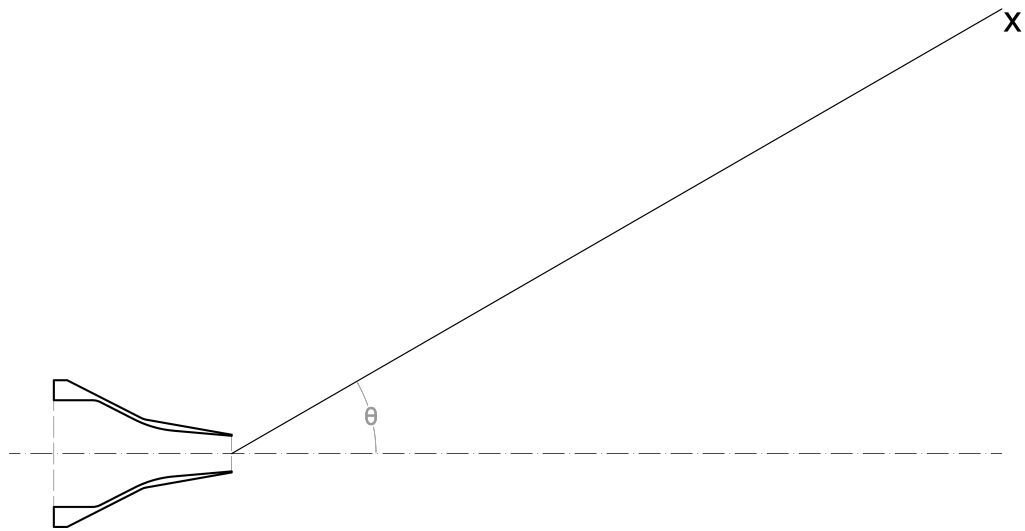


Figure 2.2: Definition of θ , the polar angle

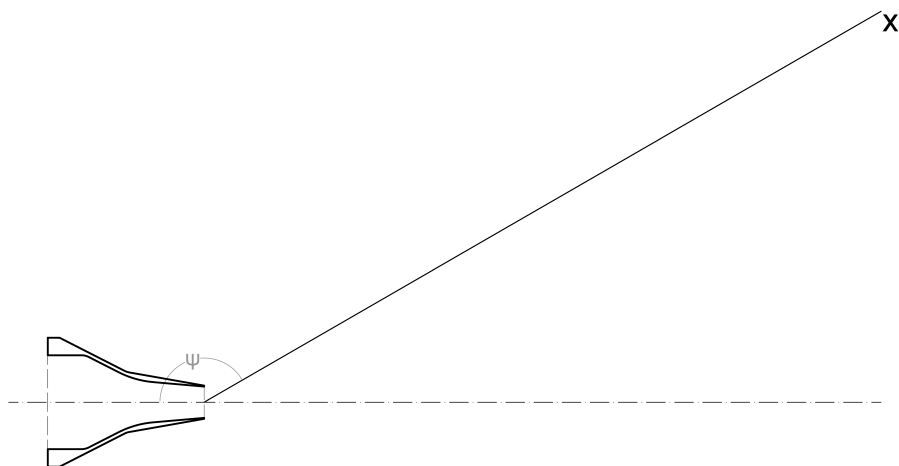


Figure 2.3: Definition of Ψ , the supplementary angle of θ

2.1.6 Total Comprehensive Model

Both mixing Noise and BBSAN are performed on the same acoustic analogy based on the LEE. Thus, the two methodologies are compatible and the results can be summed.

Combining the equation (2.32) with the equation (2.40) it is possible to evaluate the contribution to the spectral density by both BBSAN and mixing noise. The final expression is displayed hereafter.

$$\begin{aligned}
S(\mathbf{x}, \omega) = & \rho_\infty^2 a_\infty^4 \int_{-\infty}^{\infty} \int_{-\infty}^{\infty} \int_{-\infty}^{\infty} \frac{2\pi^{3/2} a_\infty^2 l_x l_y l_z x^2 \tau_s}{a_\infty^2 x^2 + (a_\infty x + \bar{u}x_1 + \bar{v}x_2 + \bar{w}x_3)^2 \tau_s^2 \omega^2} \\
& \times \left\{ \pi_g^{*0}(\mathbf{x}, \mathbf{y}, \omega) \pi_g^0(\mathbf{x}, \mathbf{y}, \omega) A_s^2 \frac{(u_s/a_\infty)^4}{\tau_s^2} + \sum_{n=1}^3 \sum_{m=1}^3 \pi_g^{*n}(\mathbf{x}, \mathbf{y}, \omega) \pi_g^m(\mathbf{x}, \mathbf{y}, \omega) \right. \\
& \times \left(B_s^2 \frac{(u_s/a_\infty)^2 u_s^2}{l_x^2} + \frac{a_{mn} K(\mathbf{y}) p_s(\mathbf{y})}{2\pi \bar{\rho}^2 \bar{u}^2 l_x^2} \int_{-k_{1min}}^{k_{1max}} \tilde{p}_s(k_1, y_2, y_3) \exp[-ik_1 y_1] dk_1 \right) \Bigg\} \\
& \times \exp \left[-\frac{\omega^2 (l_x^2 x_1^2 + l_y^2 x_2^2 + l_z^2 x_3^2)}{4a_\infty^2 x^2} \right] d\mathbf{y} \quad (2.44)
\end{aligned}$$

2.1.7 Integral Scales of Turbulence Definitions

In all spectral density equations the integral scales of turbulence are required. Jet flows exhibit self similarity and the length scale grows linearly with increasing stream-wise distance. An empirical model of the growth of the length scale with stream-wise distance might be approximated as, $l_x(y_1) = 0.138y_1 D$, where y_1 is the stream-wise distance from the nozzle exit to the source. Here, the integral scale of turbulence is found from K and ω directly from the steady RANS solution as function of Turbulent Kinetic Energy ($K(\mathbf{y})$) and of Dissipation Rate of Turbulent Kinetic Energy ($\varepsilon(\mathbf{y})$).

$$l_x(\mathbf{y}) = c_{l_{mix}} \frac{K^{3/2}(\mathbf{y})}{\varepsilon(\mathbf{y})} \quad (2.45)$$

Morris and Zaman¹⁵ examined the variation of the length scale with Strouhal number. They observed that from low to mid frequencies the integral length scale is relatively independent of St and at high frequencies the integral length scale falls off as the inverse of St. The effect of using a frequency dependent length scale for mixing noise is justified in terms of representing the physics of turbulence in jets and has improved predictions.

Referring to Miller's¹⁰ paper the expression of the frequency dependent

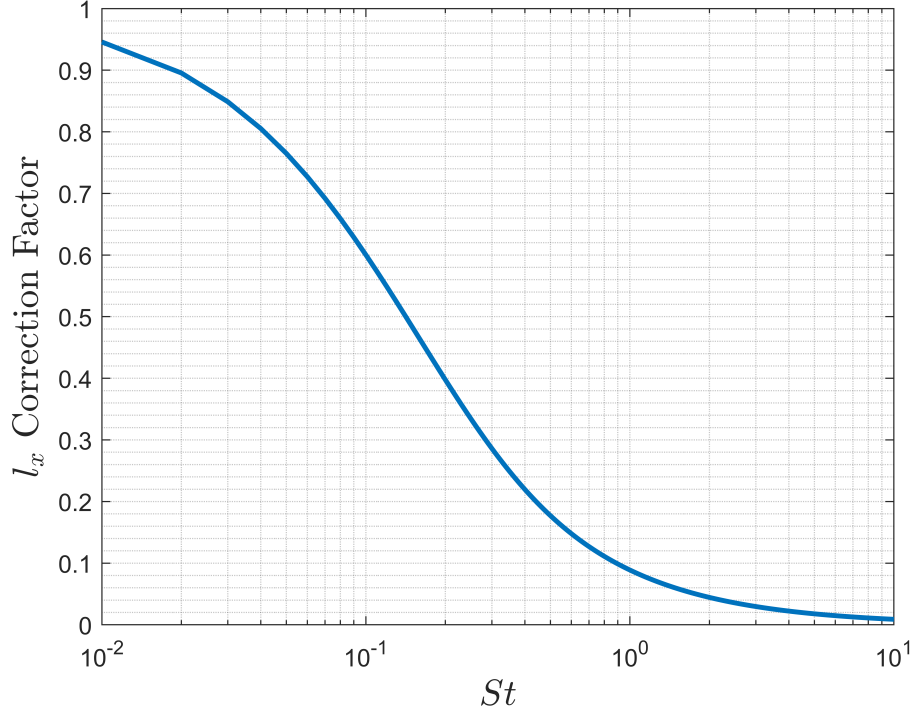


Figure 2.4: Correction factor of integral length scale due to Strouhal number

length scale is

$$l_x(\mathbf{y}, St) = l_x(\mathbf{y}) \frac{1 - \exp[-c_f St]}{c_f St} \quad (2.46)$$

where c_f is an empirical constant taken equal to 11.25 to match experimental data and St is the Strouhal number defined as

$$St = f \frac{D_2}{u_2} \quad (2.47)$$

where $f = \frac{\omega}{2\pi}$ is the frequency, D_2 is the exit jet diameter and u_2 is the exit velocity. A plot of the scaling factor with the Strouhal number is depicted in Figure 2.4. This correction is made only for characteristic length scale in the mixing noise model while in the BBSAN contribution it does not gives good predictions.

A typical acceptable value of the cross-stream length scales are the third part of the stream-wise length scale

$$l_y(\mathbf{y}, St) = l_z(\mathbf{y}, St) = \frac{1}{3} l_x(\mathbf{y}, St) \quad (2.48)$$

The temporal and velocity scales must also be related to the steady RANS solution. A simple dimensional model as done with the integral length

scale can be performed. Hence, the temporal and velocity integral scales of turbulence are

$$\tau_s(\mathbf{y}) = c_{\tau_{mix}} \frac{K(\mathbf{y})}{\varepsilon(\mathbf{y})} \quad (2.49)$$

$$u_s(\mathbf{y}) = u_{s_{mix}} \sqrt{\frac{2}{3} K(\mathbf{y})} \quad (2.50)$$

In these equations, $c_{l_{mix}}$, $c_{\tau_{mix}}$ and $u_{s_{mix}}$ are empirical constants and are going to be calibrated by performing a parametric study relative to a single jet condition and observer angle with various sets of experimental data.

Chapter 3

Acoustic Results

The acoustic solver is tested on several cases. The table 3.1 shows the jet cases analyzed. Each row represents a case with associated design Mach number (M_d), fully expanded Mach number (M_j) and total temperature ratio (TTR). The geometry is that of the SMC000 convergent nozzle (Figure 1.2) of Bridges and Brown¹.

Observers are placed at six angles from the nozzle outlet at a distance ‘ $x = 5.08 \text{ m}$ ’.

All results are displayed in terms of SPL per unit St . The final expression is given below and all the steps to follow are described in Appendix C.

$$SPL_{p.u. St} = 10 \log_{10} \left(\frac{S(\mathbf{x}, \omega)}{p_{ref}^2} \right) + 10 \log_{10} \left(\frac{u_j}{D_j} \right) \quad (3.1)$$

The predicted SPLs at various angles of observation are compared with experimental data available in the open literature¹.

Although a simplified vector Green’s function is used, the empirical correction⁶ cause the mixing noise to scale correctly as the angle of observation changes but more developed could be made in that way. In all predictions, the mixing noise peak is estimated at a higher frequency but this could be adjusted with an optimization of the Strouhal correction model of the integral length scale. The BBSAN peak frequency is predicted fairly accurately by the model at all angles, and the amplitude is particularly in agreement, even with strong screech tones in the lateral and upstream directions.

Case	M_d	M_j	TTR
SMC0003	1.00	1.47	1.00
SMC0004	1.00	1.00	2.70
SMC0008	1.00	1.24	3.20

Table 3.1: Jet Operating Conditions

3.1 Implementation of Acoustic Solver

Both equation (2.32) and equation (2.41) are implemented in the solver. To let the calculation be independent from the CFD solution a new grid has been created and the steady RANS solution is interpolated using the inverse weighted distance method onto the new structured grid that encompasses the jet plume. A structured grid, with constant spacing between grid points, is done for two reasons. First, this method allows grid independence studies using the highly resolved CFD solution databases. Second, it simplifies the calculation of the Fourier transform of p_s , since the grid spacing is constant with respect to x , y and z . Thus, a standard discrete Fourier transform (DFT) is used. This also ensures that the radial locations of p_s and the other field variables are the same.

The variables that are interpolated onto the integration region are the one which are printed in red in the resolved equations: K , ε , p , ρ , u , v and w . Afterwards, the characteristic scales of turbulence ($l_x, l_y, l_z, \tau_s, u_s$) are worked out directly on the new grid following the strategy in the section 2.1.7. It must be stated that in order to obtain a better prediction result, different constants are used in mixing and in BBSAN models. After the comparing between the result and the experiment at $\Psi = 70^\circ$, BBSAN constants $c_{l_{BBSAN}}$ and $c_{\tau_{BBSAN}}$ are found by performing a parametric study with a constant convective Mach number. They are taken as $c_{l_{BBSAN}} = 1.75$ and $c_{\tau_{BBSAN}} = 1.55$. Their values are set as constant in all other simulations. The scaling coefficients in the BBSAN model control the shape of the spectrum and, in part, its magnitude. $c_{\tau_{BBSAN}}$ controls the relative magnitude of the spectrum and is the primary means to control the sharpness of each BBSAN peak. $c_{l_{BBSAN}}$ controls some degree the width of the peaks, the smoothness of the spectra, and the relative magnitude of the BBSAN as a function of observer angle. Increasing $c_{l_{BBSAN}}$ smooths the BBSAN peaks, increases the width of each peak in the BBSAN spectrum, and lowers the relative magnitude between the peaks and troughs. Mixing constants $c_{l_{Mixing}}$, $c_{\tau_{Mixing}}$,

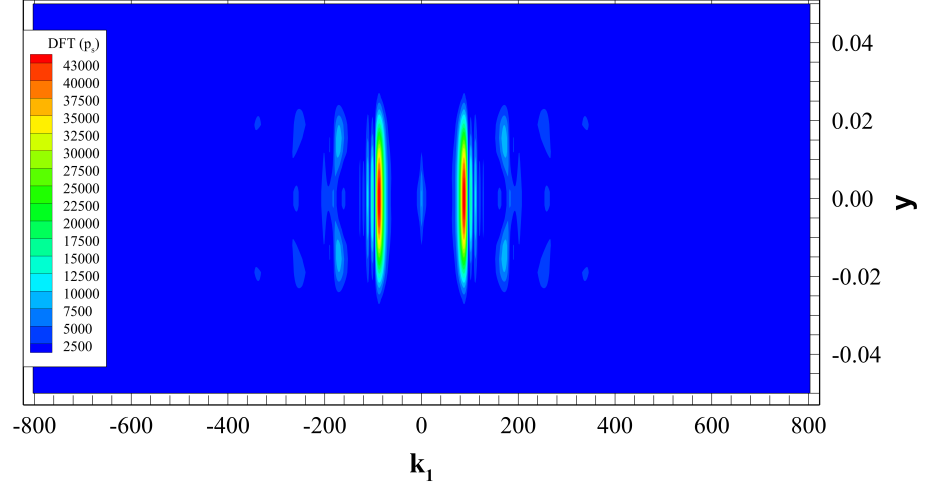


Figure 3.1: SMC0003 case - $|\tilde{p}_s|$ Magnitude of the discrete Fourier transform of shock pressure strength

c_f , A_s and B_s are chosen to be equal to the one used in the paper of Miller¹⁰ but a better result can be obtained with an adjustment of these parameters and with the implementation of a more accurate vector Green's function. The integration region is only downstream of the nozzle exit. The evaluation of the shock-associated source term requires the Proudman¹⁸ assumption for the a_{mn} term and the calculation of the Fourier transform in the axial direction of the shock pressure $p_s = p - p_\infty$. This variable is mirrored across the $x/D = 0$, so that the discrete data of p_s form an even function and a discrete Fourier transform results in a real result. The Fourier transform of the shock pressure is taken with respect to the stream-wise direction x after a Hanning window has been applied. The structured grid must have a small ' Δx ' to have a maximum representable frequency, according to Nyquist's theorem, greater than the maximum of the problem itself (f_{max}). This ensures that all aliasing problems are avoided.

$$f_{max} \leq \frac{f_{sampling}}{2} = \frac{1}{2\Delta x} \quad (3.2)$$

Values of \tilde{p}_s are real and the magnitude of the shock pressure, $|\tilde{p}_s|$, is shown in Figure 3.1 for the test case SMC0003.

It is shown that each of the peaks of the wave-number spectrum, \tilde{p}_s , contributes to peaks in the predicted BBSAN spectrum. The strongest peak in the spectrum corresponds to the fundamental shock-cell spacing and the

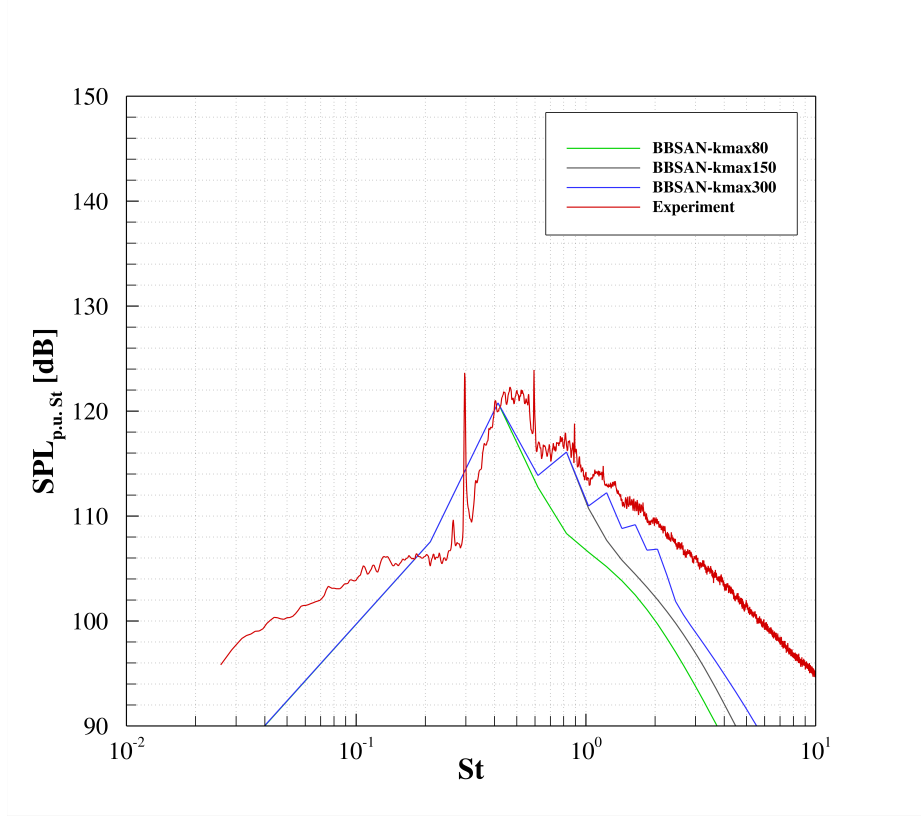


Figure 3.2: Influence of $k_{1_{max}}$ on the final result for $\Psi = 70^\circ$

subsequent peaks at higher wave-number correspond to its spatial harmonics. In fact, the integral extremes $k_{1_{min}}$ and $k_{1_{max}}$ in the equation (2.42) are chosen in order to consider all peaks. As stated also by Patel¹⁶, the low frequency components near zero wave-number are not considered inside the integration because they represent a fictitious amount of energy due to the mean flow of the RANS solution. According to this $k_{1_{min}}$ is set. With a larger value of $k_{1_{max}}$ more wave-numbers are considered in the inverse discrete Fourier transform (IDFT) but the calculation requires more time. Overall, the result is better because more spatial harmonic component are considered. An example is given in the Figure 3.2 where $k_{1_{max}}$ is increased from 80 to 300.

An additional constant, P_f , is needed in the BBSAN model to scale the amplitude of the spectral density. The scaling is the same for all jet operating conditions and a good value is $P_f = 10^{1.2} = 15.85$, the same used in the paper of Miller and Morris¹⁴.

Finally, a simplified vector Green's function is chosen but more development could be made in that way. The expression of π_g^n is reported in the Appendix B.

3.2 Case SMC0003

The SMC0003 case has $M_j = 1.47$ which means that the jet is under-expanded. In this conditions both the contribution of mixing and BBSAN could be evaluated. In the figure 3.3 is shown a comparison between acoustic predictions and experiments¹. The BBSAN is much more relevant than mixing noise upstream and at the sideline direction, while in the downstream direction, for $\Psi \geq 130^\circ$, the mixing noise is about equal to or dominates the BBSAN respectively. BBSAN contribution is predicted fairly accurately because it is not affected too much by refraction effects at small angle. As mentioned before, the simplified vector Green's function does not consider the presence of the mean flow. In fact, although the mixing noise is corrected by the factor in the equation (2.33), its contribution could be improved with a more complex Green's function as done in the work of Tam and Auriault²² or in the approach of Miller and Morris¹¹. The BBSAN component for $\Psi \geq 90^\circ$ usually over-predicts the main peak. In particular, for $\Psi = 150^\circ$, results do not match the experiments but this is surely due to refraction effects not taken into account in an accurate way.

3.3 Case SMC0004

The SMC0004 case has $M_j = 1.00$ which means that the jet is adapted. Under these conditions the contribution of BBSAN is not provided. In the figure 3.4 is shown a comparison between acoustic predictions and experiments¹. The mixing noise has the right intensity for the angle $\Psi = 50^\circ$, $\Psi = 130^\circ$ and $\Psi = 150^\circ$. For $70^\circ \leq \Psi \leq 110^\circ$ the maximum value is over-predicted by the model. Also in this case, predictions can be improved providing an optimization of the tuning parameters of the mixing model and developing vector Green's function solver taking into account refraction effects due to the mean flow.

3.4 Case SMC0008

The SMC0008 case has $M_j = 1.24$ and $TTR = 3.20$. The nozzle is operating in under-expanded condition as well. The shock cell structures in this case have less strength than the SMC0003 case and the mixing component is dominated by BBSAN only for $\Psi \leq 70^\circ$. In all other cases the mixing noise is dominant. The BBSAN model is able to catch the magnitude and frequency peak at all angle pretty well. Only for $\Psi = 110^\circ$ the BBSAN over-estimate the peak value. As described for the case SMC0004, the mixing noise model is able to quantify magnitude at some angles but overestimates it at others. Also the directivity can be adjusted with the same fixes.

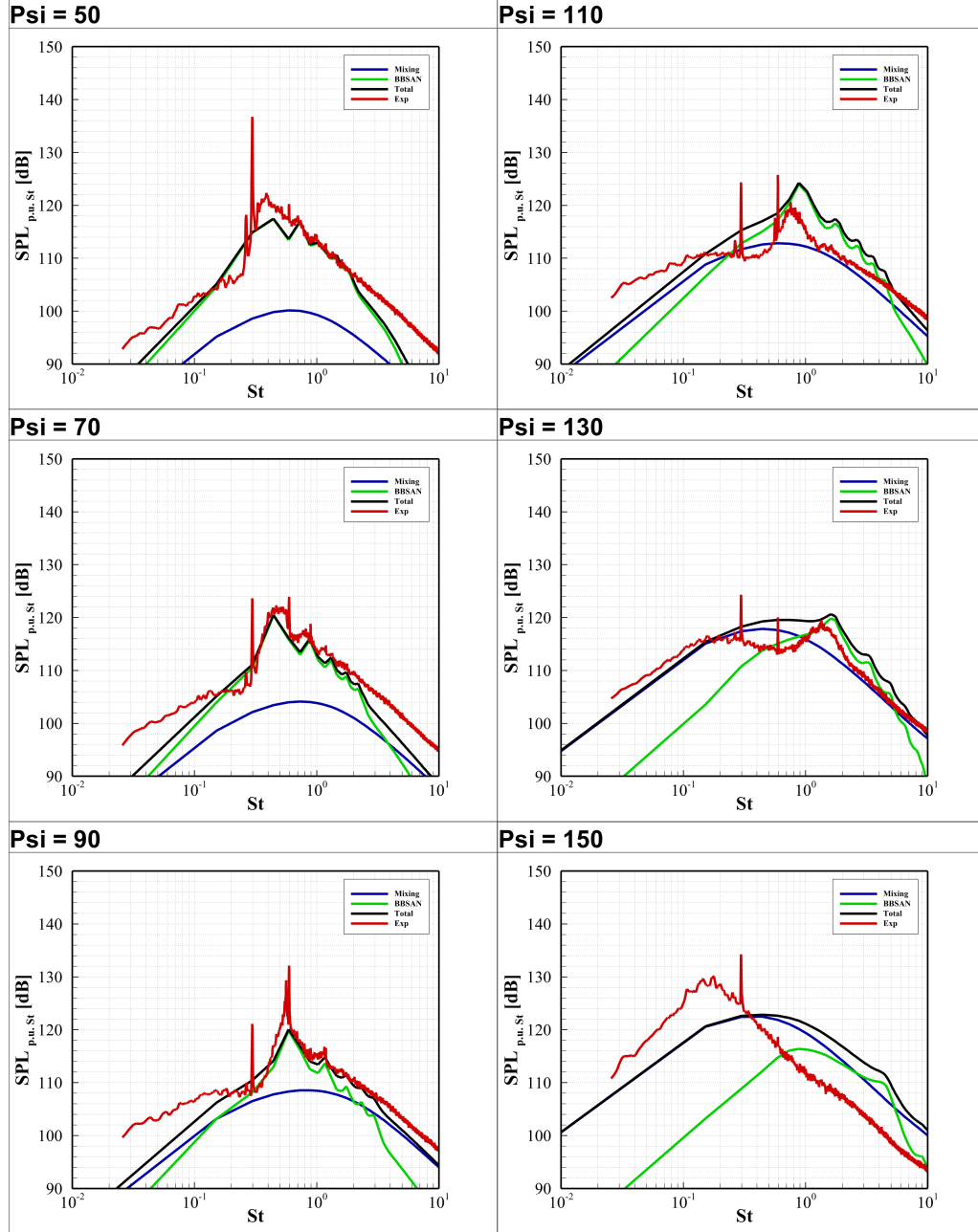


Figure 3.3: Case SMC0003 - Comparison of predictions with experiment¹ of the SMC000 convergent nozzle operating at $Mj = 1.47$ and $TTR = 1.00$ at a distance of $R/D = 100$ and angles Ψ

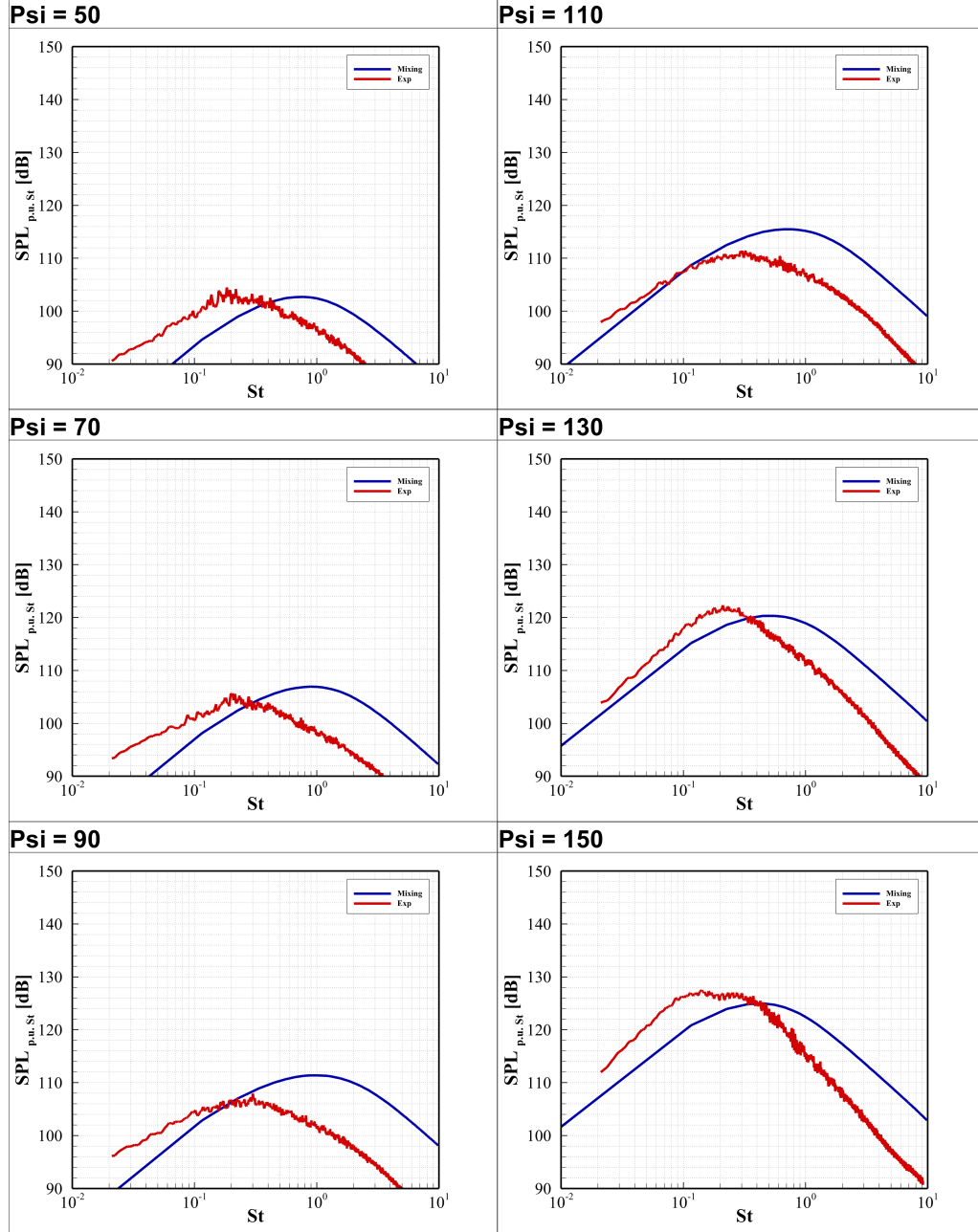


Figure 3.4: Case SMC0004 - Comparison of predictions with experiment¹ of the SMC000 convergent nozzle operating at $Mj = 1.00$ and $TTR = 2.70$ at a distance of $R/D = 100$ and angles Ψ

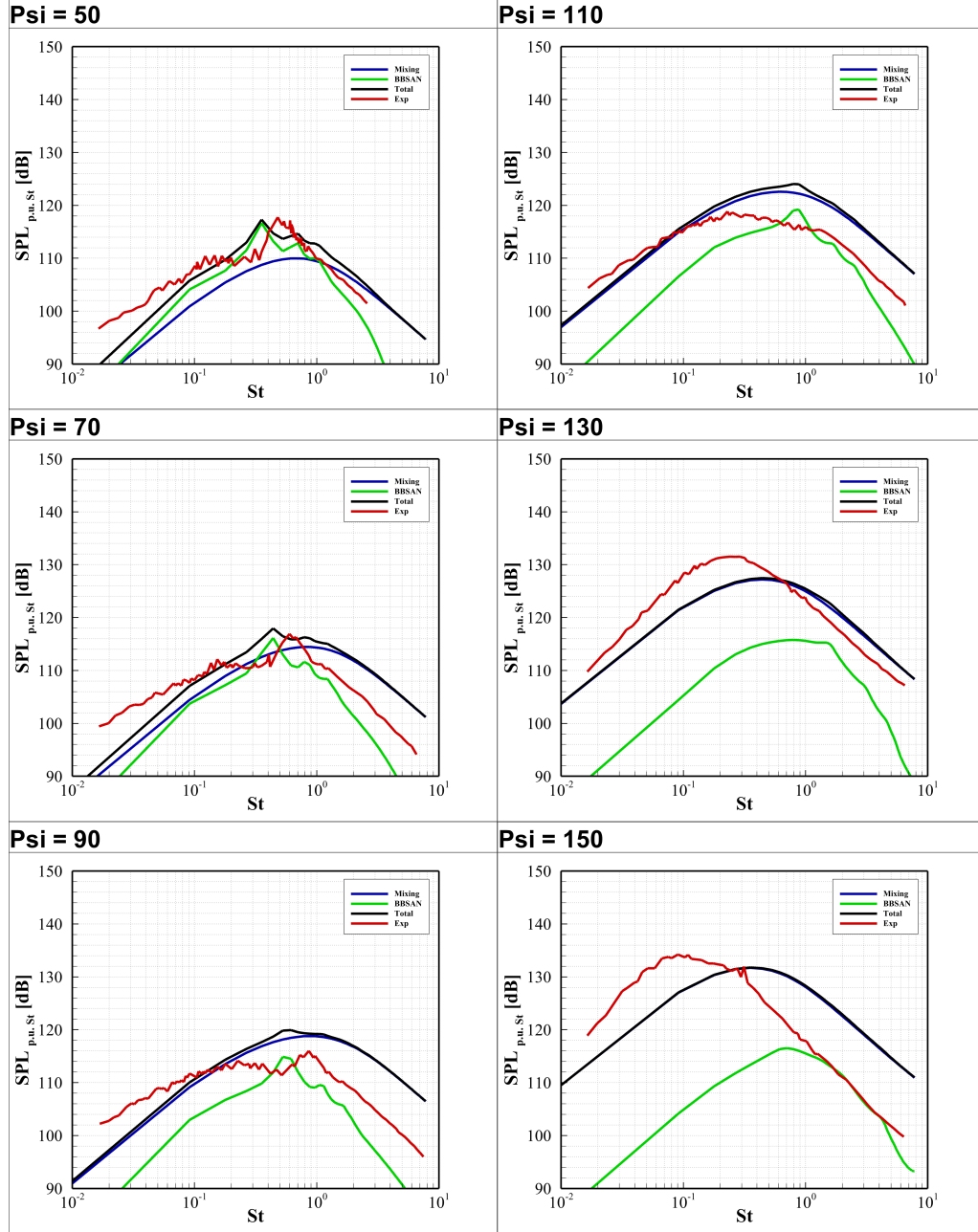


Figure 3.5: Case SMC0008 - Comparison of predictions with experiment¹ of the SMC000 convergent nozzle operating at $Mj = 1.24$ and $TTR = 3.20$ at a distance of $R/D = 100$ and angles Ψ

Conclusion and Future Works

The Euler equations are rearranged into an acoustic analogy with arguments consisting of the vector Green's function of inhomogeneous Helmholtz equation, two-point second order cross-correlation of the equivalent sources, and a steady RANS solution. The equivalent sources are modeled for jet mixing noise following the work of Tam and Auriault²³ and Morris and Boluriaan¹² and for BBSAN following the work of Morris and Miller¹⁴. A statistical model of the two-point cross-correlation of the velocity fluctuations is used to describe the turbulence within the jet plume. This statistical source model is shared between the mixing and BBSAN sources. These sources do not account for the discrete component of shock-associated noise (screeches). Propagation effects are taken into account with a simplified vector Green's function which does not consider the refraction effects due to the mean flow. A single model equation is evaluated for the mixing noise, and BBSAN in different operating conditions. The predictions are compared with experiments of jets operating subsonically through supersonically and at unheated and heated temperatures. Predictions generally capture the scaling of BBSAN for the conditions examined, but some discrepancies remain in the mixing noise model that are due to the accuracy of steady RANS turbulence model closures, the equivalent sources, and the use of a simplified vector Green's function of inhomogeneous Helmholtz equation. The model makes no assumptions regarding the fine- or large-scale turbulence, self- or shear-noise, or convective amplification. Improved predictions, in particular for mixing noise, can likely be made with the use of a more complex vector Green's function of linearized Euler equations and with the optimization of the tuning parameters.

Therefore, future works could be:

- The development of a solver for calculating more complex Green's functions of linearized Euler equations in order to improve mixing noise predictions.

- The test of different closure models for the turbulence equations
- The test of different compressibility correction models related to the turbulence closure equations that may improve the shear layer of the fluid dynamics solution
- The integration of different source models into the solver that can lead to better results

Appendix A

Green's Function

If L_x is a generic linear differential operator acting on an appropriate space of functions, in the generic variable $\mathbf{x} = (x_1, \dots, x_n)$. A differential equation, which is in general partial differential, is written as follows:

$$L_x \phi(\mathbf{x}) = f(\mathbf{x}) \quad (\text{A.1})$$

The Green's function $G(\mathbf{x}, \mathbf{y})$ of the operator L_x is defined as:

$$L_x G(\mathbf{x}, \mathbf{y}) = \delta(\mathbf{x} - \mathbf{y}) \quad (\text{A.2})$$

Where δ is the 'Dirac delta function' and thanks to its property:

$$f(\mathbf{x}) = \int f(\mathbf{y}) \delta(\mathbf{x} - \mathbf{y}) d\mathbf{y} = \int f(\mathbf{y}) L_x G(\mathbf{x}, \mathbf{y}) d\mathbf{y} \quad (\text{A.3})$$

Since $f(\mathbf{x}) = L_x \phi(\mathbf{x})$, bringing L_x (acting only on \mathbf{x}) outside the integral:

$$L_x \phi(\mathbf{x}) = L_x \int f(\mathbf{y}) G(\mathbf{x}, \mathbf{y}) d\mathbf{y} \quad (\text{A.4})$$

According to this, the solution can be evaluated:

$$\phi(\mathbf{x}) = \int f(\mathbf{y}) G(\mathbf{x}, \mathbf{y}) d\mathbf{y} + q(\mathbf{x}) \quad (\text{A.5})$$

where $q(\mathbf{x})$ is a solution of the associated homogeneous equation $L_x q(\mathbf{x}) = 0$ and it is uniquely determined by the boundary conditions of the problem.

Appendix B

Green's Function of the inhomogeneous Helmholtz Equation

The inhomogeneous Helmholtz equation is the equation

$$\nabla^2 \phi(\mathbf{x}) + k^2 \phi(\mathbf{x}) = -f(\mathbf{x}) \quad (\text{B.1})$$

As seen in the equation (A.5), the solution to the inhomogeneous Helmholtz equation is the convolution.

Here, $g(\mathbf{x}, \mathbf{y})$ is the Green's function of this equation, that is, the solution to the inhomogeneous Helmholtz equation with $f(\mathbf{x})$ equaling the Dirac delta function $\delta(\mathbf{x} - \mathbf{y})$, so $g(\mathbf{x}, \mathbf{y})$ satisfies

$$\nabla^2 g(\mathbf{x}, \mathbf{y}) + k^2 g(\mathbf{x}, \mathbf{y}) = \delta(\mathbf{x} - \mathbf{y}) \quad (\text{B.2})$$

The expression for the Green's function depends on the dimension n of the space, in particular, for $(n = 3)$, one solution is

$$g(\mathbf{x}, \mathbf{y}, \omega) = -\frac{1}{4\pi|\mathbf{x} - \mathbf{y}|} \exp[-ik|\mathbf{x} - \mathbf{y}|] \quad (\text{B.3})$$

Starting from this expression and assuming that the observer is in the far-field the vector Green's function of the LEE can be analytically obtained solving the following equation based on equations (2.16) and (2.17) in the hypothesis of a quiescent environment

$$\begin{aligned} \pi_g^n(\mathbf{x}, \mathbf{y}, \omega) = \\ - \frac{\delta_{in}}{a_\infty^2} \int_{\mathbf{z}} \frac{\partial}{\partial z_i} (g(\mathbf{x}, \mathbf{z}, \omega)) \delta(\mathbf{z} - \mathbf{y}) d\mathbf{z} - \frac{\delta_{0n}}{a_\infty^2} \int_{\mathbf{z}} g(\mathbf{x}, \mathbf{z}, \omega) \delta(\mathbf{z} - \mathbf{y}) d\mathbf{z} \quad (\text{B.4}) \end{aligned}$$

Substituting the equation (B.3) in the equation above, the vector Green's function of the LEE in the absence of a mean flow and with the observer located in the far-field is obtained

$$\pi_g^n(\mathbf{x}, \mathbf{y}, \omega) = \frac{i\omega x_n}{4\pi a_\infty^3 x^2} \exp\left[\frac{-i\omega x}{a_\infty}\right] \delta_{in} + \frac{i\omega}{4\pi a_\infty^2 x} \exp\left[\frac{-i\omega x}{a_\infty}\right] \delta_{0n} \quad (\text{B.5})$$

Appendix C

How to Present Results

$S(\mathbf{x}, \omega)$, as expressed in the equation (2.21), is a power spectral density and its measurement unit is $\text{Pa}^2 \text{Hz}^{-1}$. Often, in acoustics, power spectral density is dimensionless with a reference pressure (p_{ref}) and expressed in dB Hz^{-1} . According to this, the PSD is expressed as follows:

$$PSD = 10 \log_{10} \left(\frac{1}{f} \frac{p_{RMS}^2}{p_{ref}^2} \right) = 10 \log_{10} \left(\frac{S(\mathbf{x}, \omega)}{p_{ref}^2} \right) \quad (\text{C.1})$$

For acoustic propagation in the air, the reference pressure is chosen to be $p_{ref} = 20 \mu\text{Pa}$.

However, acoustic noise is also expressed in terms of SPL.

$$SPL = 10 \log_{10} \left(\frac{p_{RMS}^2}{p_{ref}^2} \right) \quad (\text{C.2})$$

It is straightforward to find a relationship between PSD and SPL using the definitions above.

$$SPL = PSD - 10 \log_{10} \left(\frac{1}{f} \right) \quad (\text{C.3})$$

A result, in term of SPL, is measured in dB.

Usually, it is important to adimensionalize the frequency thanks to Strouhal number (St). Following this approach, the SPL per unit Strouhal is obtained:

$$SPL_{p.u. St} = 10 \log_{10} \left(\frac{1}{St} \frac{p_{RMS}^2}{p_{ref}^2} \right) \quad (\text{C.4})$$

its unit of measurement is still dB but now the results is referred to a particular non-dimensional frequency.

The output is always the $S(\mathbf{x}, \omega)$ term and the result must be expressed as

a function of this value.

$$\begin{aligned}
SPL_{p.u. St} &= 10 \log_{10} \left(\frac{p_{RMS}^{\prime 2}}{p_{ref}^2} \right) + 10 \log_{10} \left(\frac{1}{f} \right) + 10 \log_{10} \left(\frac{u_j}{D_j} \right) \\
&= 10 \log_{10} \left(\frac{1}{f} \frac{p_{RMS}^{\prime 2}}{p_{ref}^2} \right) + 10 \log_{10} \left(\frac{u_j}{D_j} \right) \\
&= PSD + 10 \log_{10} \left(\frac{u_j}{D_j} \right)
\end{aligned} \tag{C.5}$$

Combining the equation (C.5) and the equation (C.1) the final expression for $SPL_{p.u. St}$ is obtained:

$$SPL_{p.u. St} = 10 \log_{10} \left(\frac{S(\mathbf{x}, \omega)}{p_{ref}^2} \right) + 10 \log_{10} \left(\frac{u_j}{D_j} \right) \tag{C.6}$$

$SPL_{p.u. St}$ can be seen also as a PSD where frequency (f) is adimensionalized with fully expanded jet velocity (u_j) and diameter (D_j).

$$SPL_{p.u. St} = PSD^* = 10 \log_{10} \left(\frac{1}{f} \frac{u_j}{D_j} \frac{p_{RMS}^{\prime 2}}{p_{ref}^2} \right) \tag{C.7}$$

Matlab Function for BC

```

1 function [P0,Pi,T0,I,mu_ratio,uj,Dj] = BC(Md,Mj,TTR,Pinf,Tinf,Ai,At)
2 %   Input:
3 %   Md      —   Design/Throat Mach Number           [ad]
4 %   Mj      —   Fully Expanded Mach Number           [ad]
5 %   TTR     —   Total Temperature Ratio               [ad]
6 %   Pinf    —   Far-field Pressure                    [Pa]
7 %   Tinf    —   Far-field Temperature                 [K]
8 %   Ai      —   Inlet Area                             [m^2]
9 %   At      —   Throat Area                           [m^2]
10 %
11 %   Output:
12 %   P0      —   Total Pressure                        [Pa]
13 %   Pi      —   Inlet Static Pressure                 [Pa]
14 %   T0      —   Total Temperature                    [K]
15 %   I       —   Turbulence Intensity, in per cent    [ad]
16 %   mu_ratio — Viscosity Ratio                       [ad]
17 %   uj      —   Fully Expanded Jet Velocity           [m/s]
18 %   Dj      —   Fully Expanded Jet Diameter           [m]
19
20 % constants definition
21 R = 287.058; %Air Gas Constant
22 gam = 1.4; %Ratio of Specific Heats
23 delta = (gam-1)/2;
24
25 % main calculation
26 Mi = fzero(@(x) Ai/At-Md/x*((1+delta*x^2)/(1+delta*Md^2))^( ((gam+1)/2/(gam-1)) ),0.1); %Inlet Mach Number
27 NPR = (1+delta*Mj^2)^(gam/(gam-1)); %Nozzle Pressure Ratio
28 P0 = NPR*Pinf;
29 Pi = P0/(1+delta*Mi^2)^(gam/(gam-1));
30 T0 = TTR*Tinf;
31 Ti = T0/(1+delta*Mi^2); %Static Inlet Temperature
32 mu_i = sutherland(Ti); %Dynamic Viscosity
33 rhoi = Pi/Ti/R; %Inlet Density
34 I = sqrt(0.01*mu_i/1.5)*100;
35 mu_ratio = rhoi*0.005;
36 Tj = T0/(1+delta*Mj^2); %Fully Expanded Jet Temperature
37 aj = sqrt(gam*R*Tj); %Fully Expanded Jet Speed of Sound
38 uj = Mj*aj;
39 Aj = At*Md/Mj*((1+delta*Mj^2)/(1+delta*Md^2))^( ((gam+1)/2/(gam-1)) ); %Fully Expanded Area
40 Dj = sqrt(4*Aj/pi);

```

Bibliography

- ¹ James Bridges and Clifford Brown. Validation of the small hot jet acoustic rig for aeroacoustic research. In *11th AIAA/CEAS Aeroacoustics Conference*, 2005.
- ² Gary T. Chapman and Murray Tobak. *Observations, Theoretical Ideas, and Modeling of Turbulent Flows - Past, Present, and Future*, pages 19–49. Springer New York, 1985.
- ³ Leonhard Euler. Principes généraux du mouvement des fluides. *Mémoires de l'Académie des Sciences de Berlin*, 11(1):274–315, 1757.
- ⁴ Leonhard Euler. Éclaircissemens plus détaillés sur la génération et la propagation du son, et sur la formation de l'écho. *Mémoires de l'académie des sciences de Berlin*, 21(1):335–363, 1767.
- ⁵ ANSYS Inc. Fluent theory guide, 2022.
- ⁶ Max Kandula and Bruce Vu. On the scaling laws for jet noise in subsonic and supersonic flow. In *9th AIAA/CEAS Aeroacoustics Conference and Exhibit*, 2012.
- ⁷ A. Kolmogorov. The local structure of turbulence in incompressible viscous fluid for very large reynolds' numbers. *Akademiia Nauk SSSR Doklady*, 30:301–305, 1941.
- ⁸ Michael James Lighthill and Maxwell Herman Alexander Newman. On sound generated aerodynamically i. general theory. *Proceedings of the Royal Society of London. Series A. Mathematical and Physical Sciences*, 211(1107):564–587, 1952.
- ⁹ F. R. Menter. Two-equation eddy-viscosity turbulence models for engineering applications. *AIAA Journal*, 32(8):1598–1605, 1994.

- ¹⁰ Steven A. Miller. Towards a comprehensive model of jet noise using an acoustic analogy and steady rans solutions. In *19th AIAA/CEAS Aeroacoustics Conference*, 2014.
- ¹¹ Steven A. E. Miller and Philip J. Morris. The prediction of broadband shock-associated noise including propagation effects. *International Journal of Aeroacoustics*, 11(7-8):755–781, 2012.
- ¹² Philip Morris and Said Boluriaan. The prediction of jet noise from cfd data. In *10th AIAA/CEAS Aeroacoustics Conference*, 2012.
- ¹³ Philip J. Morris and F. Farassat. Acoustic analogy and alternative theories for jet noise prediction. *AIAA Journal*, 40(4):671–680, 2002.
- ¹⁴ Philip J. Morris and Steven A. E. Miller. Prediction of broadband shock-associated noise using reynolds-averaged navier-stokes computational fluid dynamics. *AIAA Journal*, 48(12):2931–2944, 2010.
- ¹⁵ Philip J. Morris and K.B.M.Q. Zaman. Velocity measurements in jets with application to noise source modeling. *Journal of Sound and Vibration*, 329(4):394–414, 2010.
- ¹⁶ Trushant K. Patel and Steven A. E. Miller. Statistical sources for broadband shock-associated noise using the navier-stokes equations. *The Journal of the Acoustical Society of America*, 146(6):4339–4351, 2019.
- ¹⁷ Alan Powell. Theory of vortex sound. *The Journal of the Acoustical Society of America*, 36(1):177–195, 1964.
- ¹⁸ I. Proudman and Geoffrey Ingram Taylor. The generation of noise by isotropic turbulence. *Proceedings of the Royal Society of London. Series A. Mathematical and Physical Sciences*, 214(1116):119–132, 1952.
- ¹⁹ Osborne Reynolds. An experimental investigation of the circumstances which determine whether the motion of water shall be direct or sinuous, and of the law of resistance in parallel channels. *Philosophical Transactions of the Royal Society of London*, 174(1):935–982, 1883.
- ²⁰ H.S. Ribner. The generation of sound by turbulent jets. In H.L. Dryden and Th. Von Kármán, editors, *Advances in Applied Mechanics*, volume 8 of *Advances in Applied Mechanics*, pages 103–182. Elsevier, 1964.

- ²¹ S. Sarkar, G. Erlebacher, M. Y. Hussaini, and H. O. Kreiss. The analysis and modelling of dilatational terms in compressible turbulence. *Journal of Fluid Mechanics*, 227:473–493, 1991.
- ²² Christopher K. W. Tam and Laurent Auriault. Mean flow refraction effects on sound radiated from localized sources in a jet. *Journal of Fluid Mechanics*, 370:149–174, 1998.
- ²³ Christopher K. W. Tam and Laurent Auriault. Jet mixing noise from fine-scale turbulence. *AIAA Journal*, 37(2):145–153, 1999.
- ²⁴ David C. Wilcox. Dilatation-dissipation corrections for advanced turbulence models. *AIAA Journal*, 30(11):2639–2646, 1992.